Ocean Engineering 363 (2026) 126609

Contents lists available at ScienceDirect

Ocean Engineering

journal homepage: www.elsevier.com/locate/oceaneng

Research paper

Evolution and pulsation of bow wave breaking of a container ship model: A phase-resolved analysis in calm water and gravity waves

Wentao Wang [a,b], Xinyi Li [a], Jianhua Wang [a], Jian Xu [c], Decheng Wan [a,*]

[a] Computational Marine Hydrodynamics Lab (CMHL), School of Ocean and Civil Engineering, Shanghai Jiao Tong University, Shanghai, China
[b] China Ship Scientific Research Center, Wuxi, China
[c] China Shipbuilding Ninth Design & Research Institute Engineering Co., Ltd., Shanghai, China

ARTICLE INFO

Keywords:
Bow wave breaking
Statistical characteristics analysis
Phase-resolved statistical analysis

ABSTRACT

This study uses high-fidelity simulation to capture KCS bow wave breaking in gravity waves. The bow wave is analyzed from Top and Bottom views to extract different breaking structures, and phase-resolved statistics quantify bow wave breaking evolution over the gravity wave cycle. At high ship speed (Fr = 0.35), wave-induced ship motion significantly modulates breaking. The bow wave spreads laterally and falls nearly vertically, suppressing secondary overturning and continuous air cavities, producing dispersed bubble clouds. The instantaneous bow wave height in a gravity wave far exceeds that in calm water. The crest peak and actual wave rise reach 2.75 and 3 times the calm-water values, respectively, and the curling tongue length is about twice that in calm water. Entangled vortex clusters promote unsteady air entrainment. At moderate ship speed (Fr = 0.26), increasing wave steepness raises bow wave height and breaking intensity, with stronger jets, splashes, and bubble oscillations, while fragmented vortices intensify overall disruption. Compared with steepness 0.0167, the 0.03 case shows a 1.4-fold increase in curling tongue length and a 2.04-fold increase in maximum underwater depth, along with a 24.5% increase in jetting intensity and a 26.3% increase in bubble cloud pulsation. This study provides a phase-resolved framework linking bow wave structure to flow dynamics, offering a quantitative basis for bow wave breaking in gravity waves.

1. Introduction

Wave breaking is a highly unsteady and complex multiscale two-phase flow characterized by turbulence, interface instability, and air entrainment (Shao et al., 2025). Compared with wave breaking in open water, the presence of a vessel introduces additional complexity. Wave breaking may occur at the bow, while in a wave field the three-dimensional ship–wave interactions further complicate the breaking process. Bow wave breaking affects ship operations by intensifying slamming pressure fluctuations (Zhang et al., 2022), increasing energy dissipation and fuel consumption (Iafrati, 2011), and influencing the hydrodynamic performance of the propulsion system (Kawabuchi et al., 2011). As a result, increasing attention has been paid to bow wave breaking. However, due to the complexity of the breaking mechanisms and the subsequent turbulent processes, detailed investigation of this phenomenon remains challenging.

Most previous studies on bow wave breaking have focused on calm-water conditions. These studies mainly rely on experimental investigations and numerical simulations. Experimental techniques commonly used to study bow wave breaking include high-speed photography, bubble detection, Laser Doppler Velocimetry (LDV), and Particle Image Velocimetry (PIV) (Pogozelski et al., 1997; Karion et al., 2004; Waniewski et al., 2001). Dong et al. (1997) reported a strong correlation between the evolution of bow wave breaking and the associated vorticity field. Roth et al. (1999) investigated the influence of turbulence at the bow wave toe on the velocity field, while Liu et al. (2022) experimentally examined the effects of trim and scale on bow wave breaking, demonstrating that trim motion enhances the intensity of the breaking process. However, detailed analysis remains challenging due to the highly stochastic and uncertain nature of wave breaking, in which small-scale structures such as droplets and cavities are difficult to resolve experimentally (Hu et al., 2023). With the development of computational fluid dynamics (CFD), more in-depth investigations of this phenomenon have become possible.

In recent years, numerous numerical approaches that balance high accuracy and computational efficiency have been introduced for the

* Corresponding author.
E-mail address: dcwan@sjtu.edu.cn (D. Wan).

https://doi.org/10.1016/j.oceaneng.2026.126609
Received 4 April 2026; Received in revised form 25 May 2026; Accepted 15 June 2026
Available online 22 June 2026

simulation of wave breaking. These include turbulence modeling methods such as Detached Eddy Simulation (DES) and Delayed Detached Eddy Simulation (DDES)(Wyatt et al., 2008); Xie et al., 2021; Wu et al., 2020). Interface-capturing techniques such as Piecewise Linear Interface Calculation (PLIC), the Level-Set method, and the Coupled Level-Set and Volume of Fluid (CLSVOF) method are also widely used (Li et al., 2025a; Wang et al., 2010; Hu et al., 2021). These methods enable the resolution of fine-scale structures, including droplets and cavities, allowing more detailed simulations of the wave breaking process. Focusing on bow wave breaking, Wilson et al. (2006) simulated the bow wave of the high-speed vessel R/V Athena I at different Froude numbers (Fr) and observed that multiple free-surface scars were generated during the breaking process at high speeds. Wang et al. (2023) investigated bow wave breaking of the KCS at different scales and analyzed the bow wave profile and sectional vorticity distribution. Wu et al. (Wu, 2022) examined the influence of trim on bow wave breaking for the DTMB 5415 model and also found that increasing bow trim enhances turbulence. Mao et al. (2025) further investigated the effect of yaw angle on bow wave breaking of the KCS, demonstrating that increasing yaw angle leads to pronounced asymmetry in the breaking process, with significantly intensified breaking on the outer side.

In recent numerical studies of this phenomenon, attention has gradually extended beyond conventional flow-field analysis to more comprehensive investigations of multiple flow characteristics, including statistical, spectral, modal, and energetic features. Liu et al. (2022) analyzed the root mean square (RMS) of bow wave height for the KCS to investigate the unsteady fluctuations of wave breaking and further explored its dynamic behavior through frequency analysis. Mao et al. (2024) and Li et al. (2025b) ˉ (Li et al., 2024) also investigated bow wave breaking using statistical and spectral analyses, identifying key dynamic time scales associated with small-scale breaking structures. Lu et al. (2024) applied Proper Orthogonal Decomposition (POD) to the wave height and velocity fields of bow wave breaking, revealing rapidly alternating high-frequency structures during the breaking process. Regarding energy characteristics, Wilson et al. (2007) examined the distribution of underwater turbulent kinetic energy and the evolution of induced vortex structures during the bow wave breaking. Li et al. (2025a) replaced the bow geometry with a wedge-shaped structure and analyzed the evolution of underwater kinetic and potential energy during bow wave breaking. Noblesse and Delhommeau (2013) also suggested that the energy associated with bow wave breaking may be related to the breaking volume.

However, in practical operating environments, ships frequently encounter waves. In waves, the bow wave pattern may change significantly, inducing stronger turbulence and potentially causing green water events. Despite its importance, studies of bow wave breaking under wave conditions remain limited, with most research focusing on ship responses and added resistance rather than the breaking process itself. Some studies have provided preliminary insights. Ye et al. (2012) found that bow wave breaking and deck wetness can induce strong nonlinear variations in motion response amplitude operators. Sun (2023) investigated the transition from bow wave formation to deck wetness events. Maxeiner(Maxeiner et al., 2011) used a two-dimensional-plus-time (2D + T) approach to study the effects of wave conditions and hull geometry on bow wave breaking through bow wave profiles. Choi et al. (Choi and Huijsmans, 2019) conducted model experiments in regular waves of different wavelengths, showing that bow wave breaking exhibits stronger periodicity and nonlinear effects on ship resistance. However, these studies have not specifically addressed the detailed flow characteristics of bow wave breaking. Therefore, the present study extends methodologies developed for calm-water bow wave breaking to investigate the phenomenon under wave conditions.

This study qualitatively and quantitatively compares bow wave breaking profiles and fluctuation intensity between calm-water and gravity-wave conditions, and explores the underlying flow mechanisms. The influence of wave steepness is also examined. This paper is organized as follows. First, the numerical method and data-processing procedures are introduced, followed by the computational setup and grid verification and validation. Then, bow wave breaking of the KCS at Fr = 0.35 is analyzed in calm water and under a wave condition with a steepness of $H/\lambda = 0.017$. Fluctuation characteristics are quantified using the RMS of bow wave elevation, and the mechanisms are interpreted via pressure fields and vortex structures. Finally, three additional wave steepnesses ($H/\lambda = 0.017$, 0.025 and 0.03) at Fr = 0.26 are considered to examine steepness effects using waveform analysis and phase-resolved statistics, with further investigation of associated variations in underwater vortex structures.

2. Numerical approach

2.1. Numerical methodology

To capture small-scale structures in wave breaking, such as overturning, jets, splashing, and underwater air entrainment, the high-fidelity DDES turbulence method is employed in this study. In addition, since ship motions in waves directly influence the overall pattern of bow wave breaking, the overset grid technique is adopted to accurately resolve the ship motion response.

The DDES approach(Spalart et al., 2006) combines the Reynolds-Averaged Navier–Stokes (RANS) method and Large Eddy Simulation (LES) through a hybrid function. This function evaluates the local turbulence length scale to determine the appropriate modeling strategy. As a result, the RANS model is applied in the near-wall region, while LES is activated in the outer region to resolve large-scale vortex structures. The RANS component is based on the SST k–ω model(Menter, 1994), which is well suited for predicting near-wall flows in the presence of solid boundaries.

The DDES model is developed based on the DES approach(Strelets, 2001). In the DES formulation, the characteristic turbulence length scale L_{DES} is defined as follows and is strongly related to the local grid size Δ.

$$L_{DES} = \min(L_{RANS}, L_{LES}) \tag{1}$$

$$L_{RANS} = \sqrt{k} \Big/ (C_\mu \omega) \tag{2}$$

$$L_{LES} = C_{DES} \Delta \tag{3}$$

In these formulations, C_{DES} and C_μ are calibrated DES model constants, and Δ represents the local grid size, indicating that the turbulence length scale in the LES region is determined by the grid resolution. In the near-wall region, when the modeled turbulence length scale is smaller than the grid scale, the RANS model is applied using wall functions, while LES is used in the outer region.

However, relying solely on the grid size to determine the switching may activate LES too early near the wall, leading to premature flow separation. To avoid this issue, the DDES method introduces a delay function f_d as follows.

$$f_d = 1 - \tanh(512 r_d^3) \tag{4}$$

$$r_d = \frac{\nu_t + \nu}{\sqrt{u_{ij} u_{ji}} \kappa^2 d^2} \tag{5}$$

Here, r_d is the delay factor, d represents the distance to the wall, ν is the turbulent viscosity, ν_t is the eddy viscosity, κ is the von Kármán constant and $\sqrt{u_{ij} u_{ji}}$ denotes the magnitude of the velocity gradient tensor.

The delay function forces $f_d = 0$ inside the boundary layer and allows it to approach 1 in separated flow regions. With the introduction of the delay function, the turbulence length scale L_{DDES} is modified as follows:

$$L_{DDES} = L_{RANS} - f_d \max(0, L_{RANS} - L_{LES}) \tag{6}$$

To accurately capture the ship motion, the overset grid technique is used. For the wave-condition simulations, the computational domain is divided into two parts: a background grid and a body-fitted ship grid. In the overset grid framework, these two grids overlap through a topological overlay, where the background grid represents the stationary domain, while the ship grid moves independently (Cheng and Wan, 2017). The overlapping region between the background grid and the ship grid is handled using the program SUGGAR++, which establishes interpolation relationships and transfers flow-field information through the domain connectivity information (DCI).

2.2. Data processing method

The data-processing procedures in this study include free-surface reconstruction and statistical analysis of bow wave breaking under calm-water and wave conditions.

During wave breaking, strong air entrainment generates complex structures such as jets, splashing droplets, and underwater cavities, resulting in multiple air-liquid interfaces at the same location. In such regions, conventional numerical wave probes may capture mixed interfaces and fail to represent the true free-surface profile. Therefore, a method is developed to extract the free-surface contour from complex wave fields at each time step as shown in Fig. 1. The wave surface elevations in the figure are nondimensionalized by the length between perpendiculars L_{PP}.

The interface is identified using the Volume of Fluid (VOF) method based on the volume fraction α, where $\alpha = 1$ represents water and $\alpha = 0$ represents air. The air-water interface is defined by the iso-surface of $\alpha = 0.5$, from which the raw free surface is extracted as shown in Fig. 1 (a).

Fig. 1 (a) shows the raw free-surface data at a representative instant, where the data points are unevenly distributed and contain mixed multi-interface information. As observed from the original data, the reconstructed free-surface shapes differ significantly between the Top and Bottom views. In the Top view, the extracted surface mainly represents crest structures associated with breaking features such as jets and droplets. In contrast, the Bottom view mainly captures trough structures related to underwater cavities, air tubes, and bubbles. To distinguish these different breaking features, a partition-based vertex query method is employed. The interface is divided into small regions according to the computational grid, and the maximum and minimum values in each region are extracted to reconstruct the air-water interface for the Top and Bottom views through interpolation. The resulting top and bottom surfaces are shown in Fig. 1(b) and (c), respectively, while the interpolated reconstructed surface is presented in Fig. 1(d). The results indicate that this method effectively separates different breaking structures while preserving the main features of the original free surface.

Based on the reconstructed free surfaces from different views, the mean and the RMS of wave heights are calculated as z_{Mean} and z_{RMS}. It should be noted that the RMS here is not of the wave height itself, but of the wave height fluctuations relative to the mean. z_{Mean} characterize the average surface elevation, while z_{RMS} quantifies the intensity of surface fluctuations.

For calm-water conditions, z_{Mean} and z_{RMS} are computed as follows, where n is the sample number, z_i is the instantaneous wave height, and L_{PP} is the length between perpendiculars of ship used for nondimensionalization.

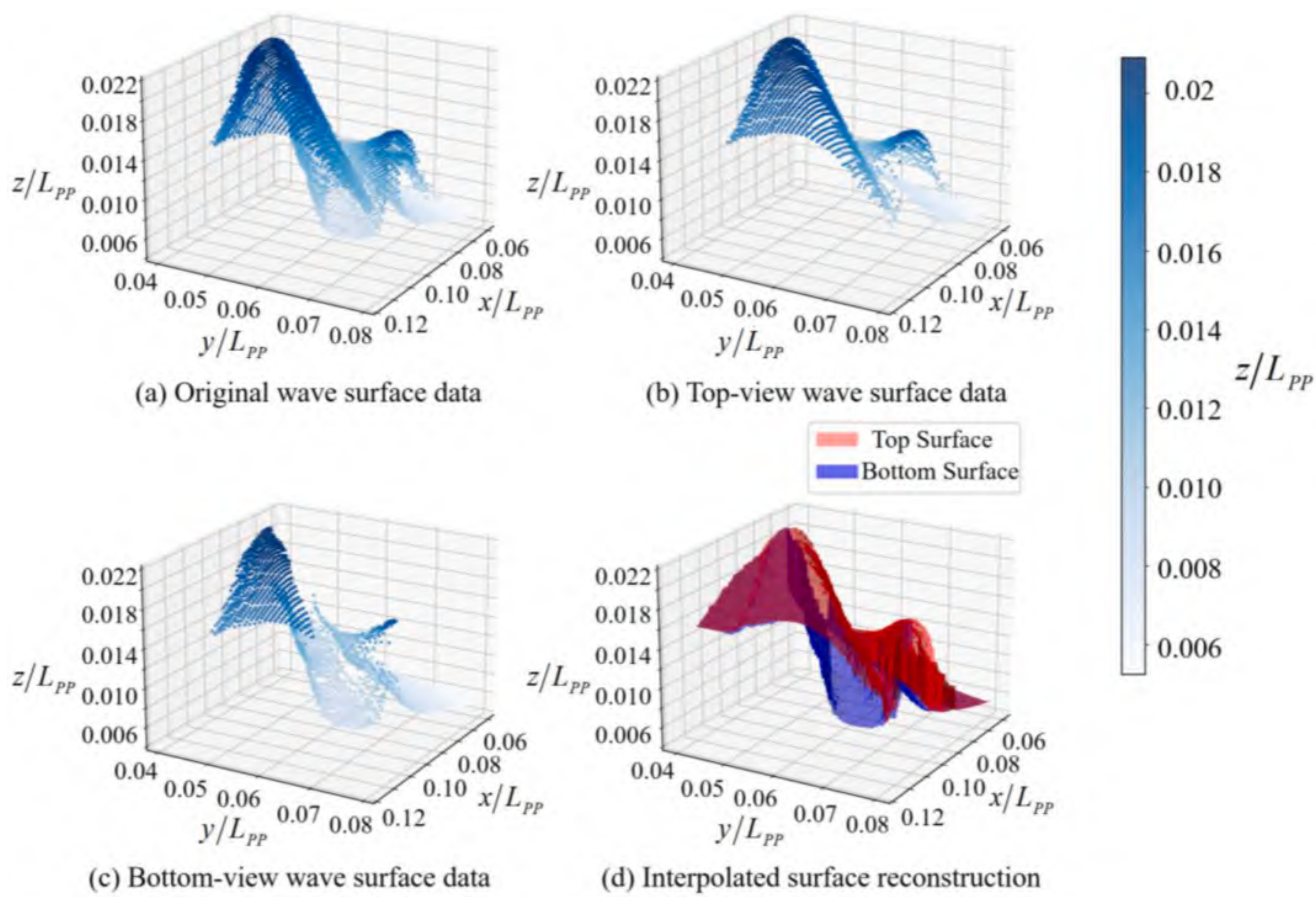

Fig. 1. Separation and reconstruction of wave breaking surfaces.

$$z_{Mean} = \frac{\sum_{i=1}^{n} (z_i / L_{PP})}{n} \tag{7}$$

$$z_{RMS} = \sqrt{\frac{\sum_{i=1}^{n} (z_i / L_{PP} - z_{Mean})^2}{n}} \tag{8}$$

However, the bow wave breaking in waves is strongly correlated with the encounter period and varies significantly within each encounter cycle. If all time instants are considered without phase distinction, the computed z_{Mean} and z_{RMS} would lose their meaning. Therefore, to account for the periodic characteristics of wave conditions, phase-resolved statistics are adopted in this section to analyze the statistical characteristics under wave conditions.

The encounter period T_e of a vessel advancing in waves is defined as:

$$T_e = \frac{2\pi}{\omega_e} \tag{9}$$

$$\omega_e = \omega - kU \cos \beta \tag{10}$$

where ω_e is the encounter angular frequency, ω is the wave angular frequency, k is the wave number, U is the speed of the ship and β is the angle between the ship's heading and the wave propagation direction. Since only head-wave conditions are considered in the present study, the encounter angular frequency reduces to:

$$\omega_e = \omega + kU \tag{11}$$

Based on T_e, time is transformed into a nondimensional phase as:

$$\phi = \frac{(t - t_{start}) \bmod T_e}{T_e} \tag{12}$$

where t denotes the instantaneous time and t_{start} represents the starting time for phase statistics. After the transformation, $\phi \in [0, 1)$ represents one complete encounter cycle. In this paper, the encounter period is divided into 36 equally spaced phase intervals, with an interval of $\Delta\phi = 1/36$. The center of each interval ϕ_i is taken as the representative phase. The i-th phase interval can then be expressed as follows.

$$\phi \in \left[\phi_i - \frac{\Delta\phi}{2}, \phi_i + \frac{\Delta\phi}{2}\right) \tag{13}$$

Based on this definition, phase-averaged wave height $z_{Mean}(\phi_i)$ and phase-resolved RMS of wave-height fluctuations $z_{RMS}(\phi_i)$ can be calculated as follows. In contrast to the calm-water statistics obtained over the entire time series, the phase-resolved statistics account for the periodic variation associated with the wave–ship encounter process.

$$z_{Mean}(\phi_i) = \frac{1}{N_i} \sum_{j=1}^{N_i} z_j \Big/ L_{PP} \tag{14}$$

$$z_{RMS}(\phi_i) = \sqrt{\frac{\sum_{j=1}^{N_i} \left(z_j / L_{PP} - z_{Mean}(\phi_i)\right)^2}{N_i}} \tag{15}$$

where N_i is the number of samples falling within the phase interval ϕ_i, and z_j is the instantaneous wave height measured within that interval.

3. Numerical setup

3.1. Geometry and numerical cases

As shown in Fig. 2, the KRISO Container Ship (KCS) model is adopted as the research object in the present study. A 6 m-scale model is employed, corresponding to a geometric scale ratio of 1:37.89. The length between perpendiculars of the model is $L_{PP} = 6.0702m$. The principal parameters of the KCS model are listed in Table 1.

The overall test conditions are summarized in Table 2. In Case2 to Case5 KCS operates in head waves. In the table, λ is the wavelength, H is the wave height, λ/L_{PP} denotes the wavelength-to-ship-length ratio, and H/λ represents the wave steepness and Fr refers to the Froude number:

$$\text{Fr} = \frac{v}{\sqrt{gL}} \tag{16}$$

where v is the ship speed, g is the gravitational acceleration, and L is the characteristic length, which is taken as L_{PP} here.

Case 1 corresponds to the calm-water condition, where the model advances at Fr = 0.35. The model attitude is fixed with a bow trim angle of 1 deg. Cases 2–5 represent wave conditions with regular waves, where the λ/L_{PP} is set to 1.15. In Case 2, the ship speed is the same as that in calm water and the wave steepness $H/\lambda = 0.017$. For Cases 3–5, a lower speed of Fr = 0.26 is selected, considering that excessively high speed may intensify green-water events on the deck under large wave steepness. The wave steepness H/λ for these three cases are 0.017, 0.025, and 0.03, respectively. Under wave conditions, the model advances in head seas and is allowed to move with two degrees of freedom, namely heave and pitch.

The density of water ρ_w and the density of air ρ_a are set to 997 kg/m^3 and 1.184 kg/m^3 respectively, and the kinematic viscosity of water ν_w and the kinematic viscosity of air ν_a are set to $1.48 \times 10^{-5} m^2/s$. The gravitational acceleration g is 9.81 m/s^2.

3.2. Computational domain and mesh

To reduce the computational cost, a half-domain configuration is adopted by exploiting the symmetry of the head-wave condition. The origin of the computational domain is defined at the intersection between the still-water free surface and the forward perpendicular (FP) of the KCS model. The positive x-axis is oriented from the bow toward the stern, the positive y-axis points from the centerline toward the starboard side, and the positive z-axis is defined vertically upward. The overall computational domain is illustrated in Fig. 3.

Table 1
Main parameters of KCS.

Parameters	Value
Scale ratio λ	37.89 (–)
Length between perpendiculars L_{PP}	6.0702 (m)
Breadth B	0.8498 (m)
Draft T	0.2850 (m)
Displacement ∇	0.9399 (m^3)
Wetted surface area w/o rudder S_W	6.6177 (m^2)
Wetted surface area of rudder S_R	6.6177 (m^2)

Fig. 2. Geometry of KCS model.

Table 2
Test conditions and model configurations.

Cases	Environment	λ/L_{PP}	H/λ	Fr	Trim Angle (∘)	Motion condition
Case1	Calm water	—	—	0.35	1	Fixed
Case2	Wave	1.15	0.017		—	Free to pitch and heave
Case3			0.017	0.26		
Case4			0.025			
Case5			0.030			

For the wave cases, the entire computational domain translates forward with the velocity of the advancing ship. The length, width, and height of the domain are 5λ, 2λ and $2L_{PP}$ respectively. The inlet boundary is located 1.2λ upstream of the FP. The wave generation zone is arranged at the inlet, covering a length of λ, with its tail boundary located 0.2λ from the FP. This setup is designed to generate stable waves and ensure their effective propagation to the ship. A damping zone with a length of 1.5λ is arranged at the outlet, effectively suppressing wave reflection and minimizing its impact on the wave environment. The distance from the wave generation zone to the damping zone is 2.5λ, corresponding to approximately $2.875L_{PP}$. This spacing allows the ship-generated waves to fully develop. The atmosphere and bottom boundaries are placed $0.5L_{PP}$ above and $1.5L_{PP}$ below the still-water level, respectively, satisfying the deep-water condition.

The overset grid region, shown as the black box surrounding the hull, spans $x \in [-0.2L_{PP}, 1.2L_{PP}]$, $y \in [0, 0.3L_{PP}]$ and $z \in [-0.18L_{PP}, 0.18L_{PP}]$. This region fully encloses the hull and provides sufficient space for interpolation and data exchange with the background grid. For the boundary setup, the inlet is defined as a wave-generation velocity inlet, while the outlet is treated as a multiphase pressure outlet. The atmosphere boundary is specified as a pressure outlet, the left plane is set as a symmetry plane, and the ship hull is treated as a no-slip wall.

For the calm-water condition, the computational domain remains the same, except that the inlet velocity is set equal to the ship speed and the ship model is fixed, with the entire computational domain employing a relative coordinate system.

The computational mesh arrangement is shown in Fig. 4, and the refinement regions are summarized in Table 3. To control computational cost, a graded mesh distribution is employed, with relatively coarse resolution applied in the near-bottom region and within the damping zone. The mesh is progressively refined toward the ship hull to accurately capture ship motions and free-surface evolution.

As shown in Fig. 4(a) and (b), the mesh distribution around the hull and near the free surface is illustrated, respectively. Each increase in refinement level corresponds to halving the mesh size in all spatial directions. As shown in Table 3, Region 4 is a refinement zone designed to resolve regular waves. Its grid resolution is influenced by the number of vertically refined layers within the regular wave height. Given that the refinement level of region 4 is fixed at 2, variations in the number of vertical refinement layers lead to different base cell sizes for region 0. Consequently, the background grid is also determined by the regular wave height and the number of vertical refinement layers. Regions 1, 3, and 5 are refinement zones around the hull, used to resolve ship motions. Region 2 is the overset interpolation region, enabling data exchange between the moving ship grid and the background grid. Region 6 is a highly refined zone dedicated to capturing the generation and breaking of bow waves.

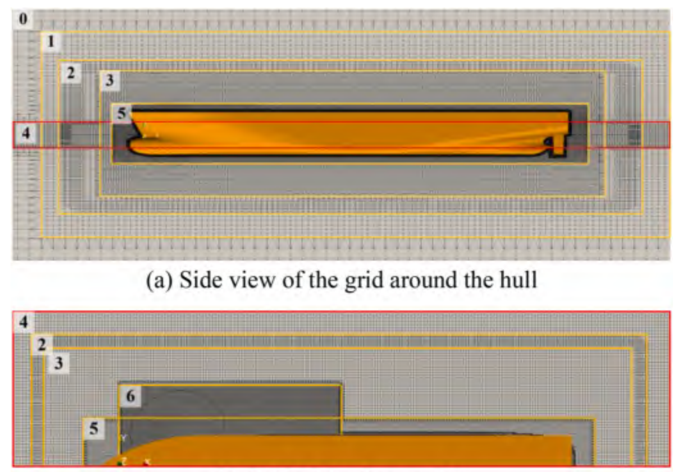

(a) Side view of the grid around the hull
(b) Grid of the free surface

Fig. 4. Computational grid arrangement.

Table 3
Mesh refinement levels.

Refinement region ID	Refinement region	Refinement level
0	Background mesh	0:0:0
1	Hull refinement region 1	1:1:1
2	Overset interpolation region	1:1:1
3	Hull refinement region 2	2:2:2
4	Regular-wave-height region	2:2:2
5	Hull refinement region 3	3:3:3
6	Bow wave-breaking region	4:4:4

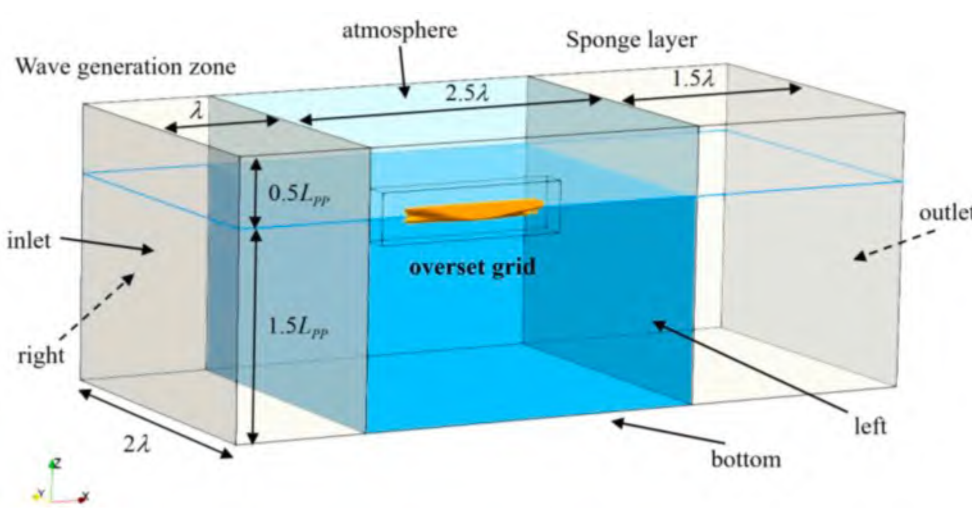

Fig. 3. Computational domain setup.

3.3. Verification and validation

3.3.1. Wave generation verification

Given that the mesh refinement requirements in the wave height region vary with wave steepness, empty-domain verifications are conducted for regular waves with steepnesses of 0.017, 0.025, and 0.03. The verification domain is set up identically to the ship-containing configuration, except that the ship model is removed. The verification covers both temporal and spatial aspects, achieved by deploying numerical wave probes in the flow field. The temporal verification is based on the free-surface elevation time history at the bow position (x = 0), while the spatial verification is performed by comparing the wave profiles at a given instant.

During wave propagation, numerical dissipation is inevitable. To mitigate its effects, both the horizontal and vertical grid spacing within the wave height range should satisfy accuracy requirements. Based on experience from previous studies, the horizontal grid size Δx is controlled to be three times the vertical grid size Δz, and different mesh resolutions are constructed by varying the Δz. In the empty-domain verification, the time step is determined based on a Courant number of 0.1. Figs. 5–7 present the empty-domain verification results for regular waves with steepnesses of 0.017, 0.025, and 0.03, respectively. In each figure, the subfigure (a) shows the wave elevation time history at x = 0, used to evaluate the temporal stability of wave propagation. The subfigure (b) presents the spatial wave profile along the y = 0 cross-section after five wave periods of development, used to assess the spatial stability of wave propagation.

For regular waves with steepnesses of 0.017 and 0.025, the vertical grid spacing within the wave height range is set as $\Delta z = H/5$, $H/10$, and $H/15$, corresponding to coarse, medium, and fine meshes, respectively. The two cases exhibit similar grid convergence behavior. As shown in Figs. 5 (a) and Fig. 6 (a), at $\Delta z = H/5$, the wave amplitude decays significantly during propagation. When the mesh is refined to $\Delta z = H/10$ and $\Delta z = H/15$, the numerical and theoretical solutions agree well, indicating good temporal stability. From Figs. 5 (b) and Fig. 6 (b), spatial attenuation decreases with mesh refinement. At $\Delta z = H/5$, considerable attenuation occurs. At $\Delta z = H/10$, slight attenuation remains, and at $\Delta z = H/15$, almost no attenuation is observed.

The maximum relative error and the grid convergence index (GCI) are further evaluated in Tables 4 and 5. With mesh refinement, the maximum relative error decreases rapidly. Using the medium mesh, all deviations are within 4%, indicating good accuracy. Meanwhile, the GCI values also decrease with refinement and is generally below 5%. In the few cases, it slightly exceeds 5% but remains close. Therefore, convergence is considered satisfactory under the present mesh strategy. Consequently, for wave steepnesses of 0.017 and 0.025, the refinement scheme of $\Delta z = H/10$ is ultimately adopted.

For the regular wave with a steepness of 0.03, the vertical grid spacing Δz within the wave-height region is set as $H/5$, $H/10$, $H/15$, and $H/20$, corresponding to coarse, medium, medium-fine, and fine meshes, respectively. As shown in Fig. 7(a), when the mesh is refined to $\Delta z = H/15$, the simulated wave height nearly coincides with the theoretical solution. Further refinement to $\Delta z = H/20$ yields no significant improvement. From Fig. 7 (b), as the free-surface grid resolution increases, the spatial attenuation of wave amplitude gradually decreases. At $\Delta z = H/10$, the attenuation already approaches that at $\Delta z = H/15$, indicating diminishing returns with further mesh refinement.

Similarly, the maximum relative error and the GCI between the simulated and theoretical values are evaluated for the medium, medium-fine, and fine meshes. The results are listed in Table 6. With mesh refinement, the maximum relative error decreases rapidly. For the medium-fine mesh, deviations from the theoretical values are within 4%, indicating good accuracy. The GCI also decreases and remains below 5%, demonstrating satisfactory convergence under the present mesh strategy. Therefore, for the regular wave with a steepness of 0.03, $\Delta z = H/15$ is adopted.

3.3.2. Wave-condition validation

For the wave condition, Case 3 is selected for numerical validation of KCS bow wave breaking in waves. The experimental data used for mesh validation are sourced from the 2015 Tokyo Workshop (Hino et al., 2020), while the CFD reference results are taken from the numerical study by Guo et al. (2023). Based on the empty-domain verification, a vertical resolution of $\Delta z = H/10$ is adopted. The mesh count for Case 3 is approximately 9.36 million, and excluding the boundary layer, the minimum grid size is about 0.006 m. The corresponding heave and pitch responses are shown in Fig. 8.

It can be observed that the present simulation results for both heave and pitch are closer to the experimental data than the CFD reference results, indicating that the overset grid achieves satisfactory interpolation accuracy under the current mesh strategy. The mean relative error of the heave response is approximately 4.95% at the crests and 4.53% at the troughs. For the pitch response, the corresponding errors are 1.95% at the crests and 1.70% at the troughs. These error levels are within an acceptable range, demonstrating that the selected mesh can reliably reproduce the ship motion responses in waves.

In addition, the time history of the resistance coefficient is presented in Fig. 9. Since only the mean value is available from the experiment, it is represented by a horizontal line. The black solid line denotes the simulated time history, while the blue open circles indicate the experimental mean resistance coefficient of 7.11×10^{-3}. The red dashed line represents the mean of the simulated resistance coefficient, which is about 7.42×10^{-3}. The relative error between the simulation and

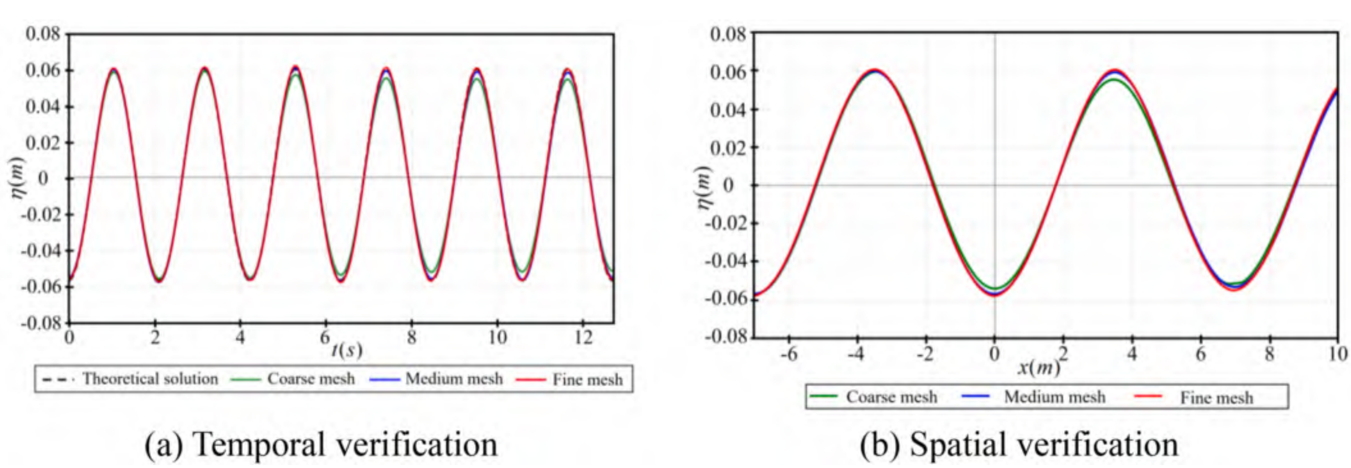

Fig. 5. Wave generation verification ($H/\lambda = 0.017$).

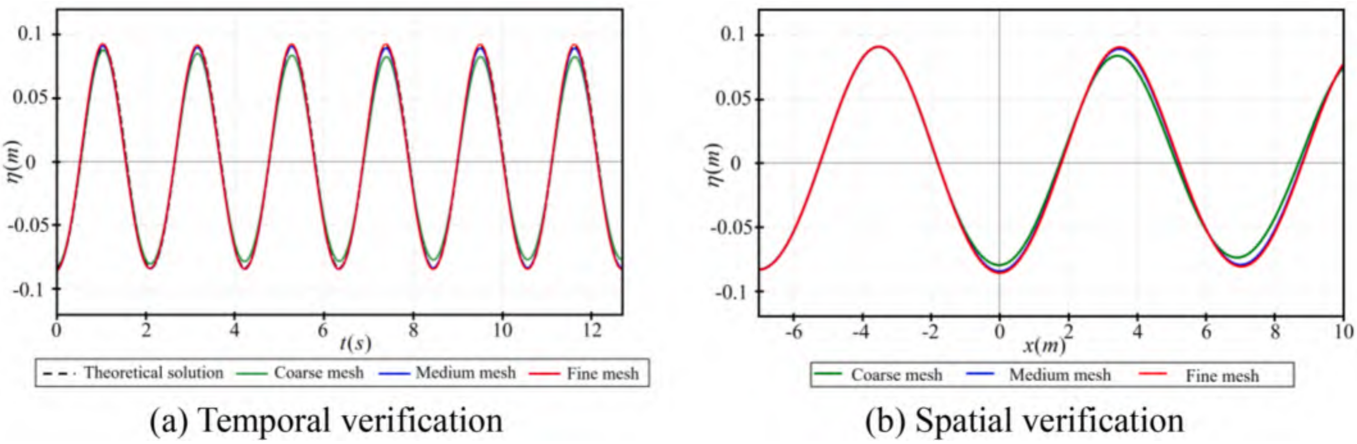

Fig. 6. Wave generation verification ($H/\lambda = 0.025$).

Table 4
Maximum error and GCI calculation of case with $\boldsymbol{H/\lambda} = 0.0167$

Mesh	Number of cells (Million)	Max Temporal Error (%)	Temporal GCI (%)	Max Spatial Error (%)	Spatial GCI (%)
Coarse	1.06	9.668	—	8.523	—
Medium	5.12	3.570	4.429	2.432	5.531
Fine	9.80	0.930	2.820	0.502	3.371

Table 5
Maximum error and GCI calculation of case with $\boldsymbol{H/\lambda} = 0.0167$

Mesh	Number of cells (Million)	Max Temporal Error (%)	Temporal GCI (%)	Max Spatial Error (%)	Spatial GCI (%)
Coarse	0.92	10.323	—	9.595	—
Medium	3.56	3.632	4.605	3.785	5.033
Fine	7.81	2.259	2.463	1.847	2.840

experiment is approximately 4.36%, which falls within an acceptable range, indicating satisfactory accuracy.

In summary, the present mesh refinement strategy demonstrates satisfactory performance in empty-domain wave generation, ship motions and resistance in waves, as well as hydrodynamic characteristics under calm-water conditions. Therefore, the meshes for all cases in this study are constructed based on the vertical free-surface resolution determined from the empty-domain wave-generation verification, together with the refinement regions defined in Table 3.

3.3.3. Calm-water validation

Based on the selected mesh, the KCS model at Fr = 0.35 with a fixed trim of 1° by the bow is simulated under calm-water conditions to validate the hydrodynamic coefficients. The experimental data are taken from the 2025 International CFD Conference.

Table 7 presents the hydrodynamic coefficients obtained from the simulation and the experiment, including the resistance coefficient C_T, lift coefficient C_L, and pitch moment coefficient C_{MY}. The simulated hydrodynamic coefficients agree well with the experiments. The largest relative error observed in the pitch moment coefficient C_{MY} is −3.38%, which remains within an acceptable range. The selected mesh is also considered sufficiently accurate for calm-water simulations.

Table 6
Maximum error and GCI calculation of case with $\boldsymbol{H/\lambda} = 0.0167$

Mesh	Number of cells (Million)	Max Temporal Error (%)	Temporal GCI (%)	Max Spatial Error (%)	Spatial GCI (%)
Medium	119	8.345	—	8.254	—
Medium-fine	451	3.796	4.986	3.914	4.994
Fine	920	1.507	1.336	2.677	3.322

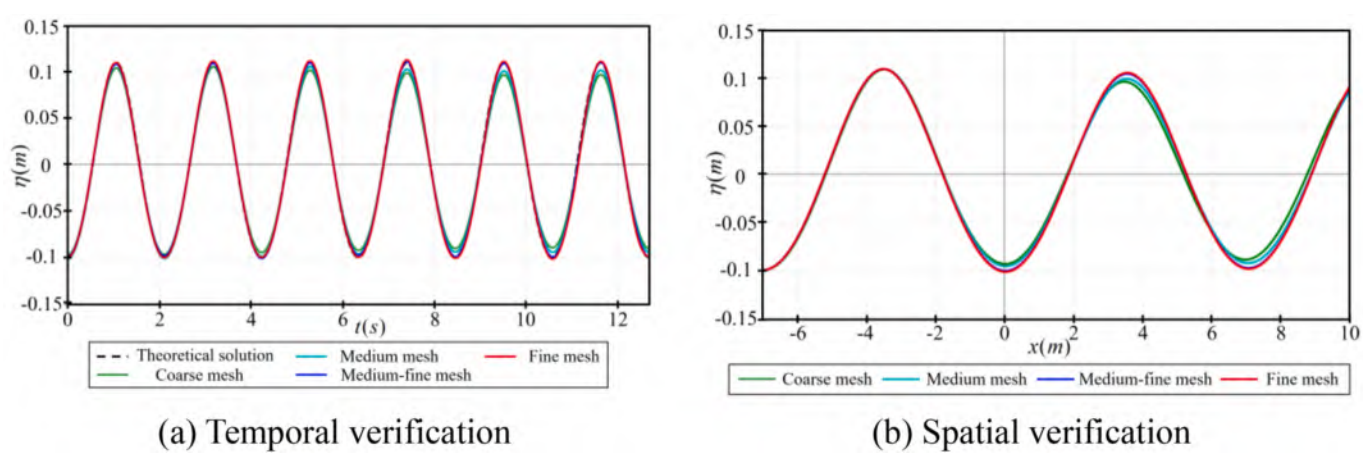

Fig. 7. Wave generation verification ($H/\lambda = 0.03$).

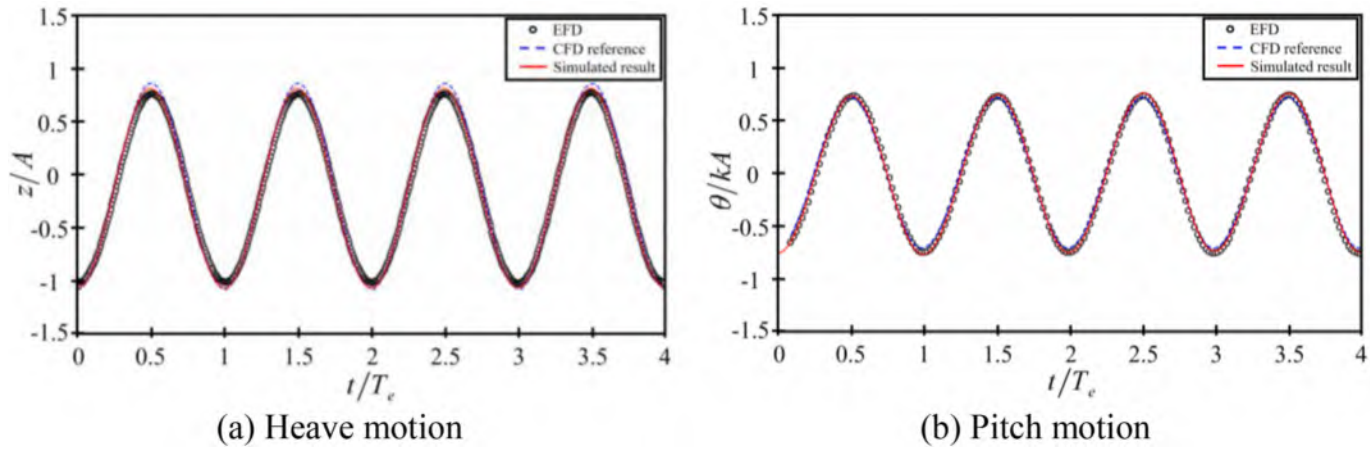

Fig. 8. Validation of ship motions in waves.

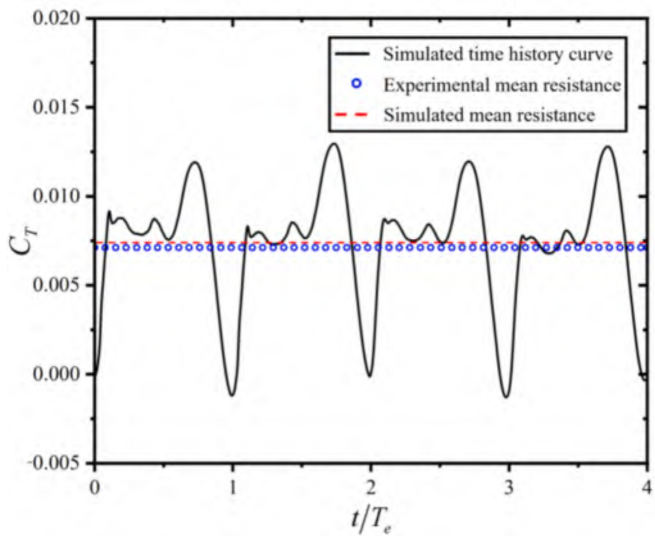

Fig. 9. Validation of ship resistance in waves.

Table 7
Validation for hydrodynamic coefficients in calm water.

Hydrodynamic coefficients	EFD	CFD	Relative error (%)
1000 C_T	5.716	5.663	−0.93
1000 C_L	346.773	353.250	1.87
1000 C_{MY}	1.154	1.115	−3.38

4. Results and discussion

4.1. Bow wave breaking under calm water and wave environments

4.1.1. Bow wave evolution

Based on the mesh strategy, Case 1 and Case 2 are selected to compare the bow wave breaking of KCS. Fig. 10 shows the bow wave evolution for Case 1 in calm water, while Figs. 11 and 12 show the corresponding results in the wave condition of Case 2. In this study, $t/T_e = \frac{1}{4}$ corresponds to the instant when the wave crest reaches the bow, while $t/T_e = \frac{3}{4}$ corresponds to the arrival of the wave trough. Fig. 11 shows only the overall wave surface at the instant $t/T_e = \frac{1}{4}$, with white areas indicating grid overlap. For wave profiles, eight representative instants are selected within one encounter period at intervals of $\frac{1}{8}T_e$ in Fig. 12. Instantaneous wave profiles along axial sections are extracted and plotted as black solid lines. The axial range is $x \in [0.02L_{PP}, 0.4L_{PP}]$, with a spacing of 0.02 L_{PP}.

Figs. 10(b) and 11 present the difference in overall wave surface between calm water and wave conditions at the typical instant $t/T_e = \frac{1}{4}$. At wave crest encounter, bow wave breaking in the gravity wave is more pronounced. The wave height is much larger than that in calm water, and the wave shape changes dramatically. The initial overturning dominates with stronger secondary jets and splashes, while the induced secondary overturning becomes less noticeable.

Further comparison between Figs. 10(b) and 12 shows that in calm water two air-entrainment regions form, with cavities extending downstream as continuous tubes. In the wave, however, the breaking patterns are modulated by wave periodicity and ship motions. At $t/T_e = 0$, only a single, more unsteady plunging occurs, producing a slender jet with little air entrainment. At $t/T_e = \frac{1}{8}$, bow-down motion increases overturning bow wave height. The water sheet becomes thinner and more stretched, fragmenting more into jets and droplets, and evolves laterally rather than downward. The most intense breaking occurs between $t/T_e = \frac{1}{4}$ and $t/T_e = \frac{1}{2}$. Near the bow, the wave front rises steeply and narrowly, with jets breaking violently into droplets. In the mid-bow region, broken water sheets overturn downward, generating unsteady secondary breaking. Air entrainment appears as dispersed bubble clouds rather than coherent cavities, and overall entrainment is weaker than in calm water. Between $t/T_e = \frac{5}{8}$ and $t/T_e = \frac{3}{4}$, limited entrainment and weak free-surface scars are observed. At $t/T_e = \frac{7}{8}$, slight plunging returns near the bow front, and a localized overturning forms along the ship side, starting the next breaking cycle.

4.1.2. Bow wave height and pulsation

Based on the above comparisons, phase-resolved wave-height statistics of KCS bow wave breaking in waves are evaluated using Eqs. (7), (8) and (14)-(15) and compared with calm-water results. Calm-water statistics come from continuous time series and represent temporal fluctuations, while wave statistics come from phase-aligned sampling over multiple cycles and reflect cycle-to-cycle variability. Therefore, the RMS values are not strictly comparable. Only wave elevation is quantitatively compared; breaking intensity is discussed qualitatively. Fig. 13 shows calm-water wave-height statistics, while Figs. 14 and 15 show phase-resolved results in the wave. The color scale for the z_{Mean} in calm water and the $z_{Mean}(\phi_i)$ in waves, is set to −0.04 - 0.06. The RMS range is set to 0 - 0.005 for calm water z_{RMS} and the Bottom-view $z_{RMS}(\phi_i)$ in the wave, and 0 - 0.018 for the Top-view $z_{RMS}(\phi_i)$ in the wave. Four representative instants $t = 0, \frac{T_e}{4}, \frac{T_e}{2}, \frac{3T_e}{4}$ are considered, corresponding to the phases $\phi_i = 0$, 0.25, 0.5 and 0.75.

Figs. 13(a) and 14 show clear differences from the Top view between the two cases. The contours of z_{Mean} and $z_{Mean}(\phi_i)$ show that at the

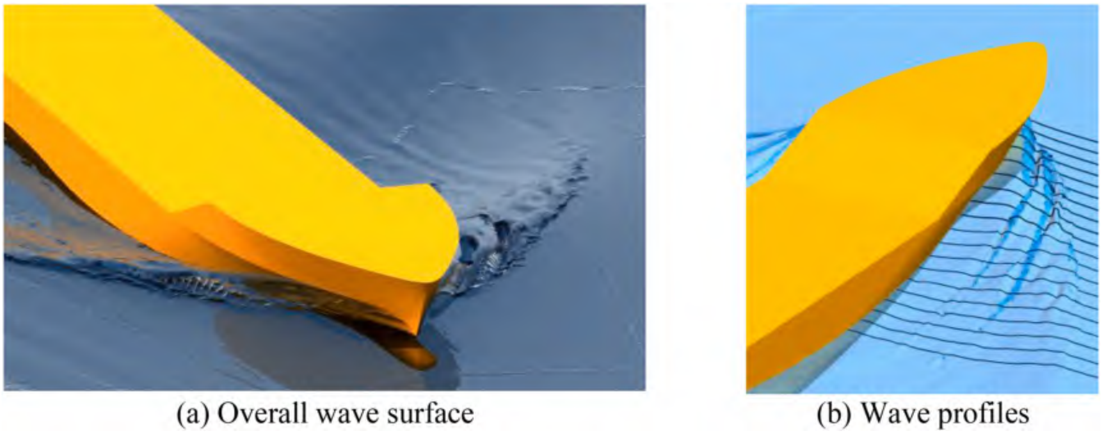

Fig. 10. Bow wave breaking evolution of KCS with 1° trim in calm water.

Fig. 11. Instantaneous wave surface of KCS wave breaking at wave crest encounter.

beginning of the encounter period, both the wave spreading angle and transverse range under wave conditions are smaller than those in calm water. As the phase increases, both gradually enlarge and exceed the calm-water values at $\phi_3 = 0.5$, indicating that waves significantly modulate the wave pattern. In the initial overturning region, the overturning steepness under wave conditions is much higher than that in calm water. Regarding wave height evolution, from $\phi_1 = 0$ and $\phi_2 = 0.25$, which corresponds to the wave crest encounter, wave height increases rapidly and is much larger than that in calm water. Later, during the transition to the wave trough, wave height decays quickly while the crest expands outward, and the maximum wave height drops rapidly, eventually becoming lower than that in calm water. The mean wave height contour further clarifies that initial overturning breaking dominates under wave conditions, whereas the height difference between initial and secondary overturning is relatively small in calm water. Under wave conditions, the wave height of secondary overturning is significantly smaller than that of initial overturning. The z_{RMS} and $z_{RMS}(\phi_i)$ contours indicate that in calm water, the regions of intense wave breaking from the Top view are mainly distributed along the edge of secondary overturning, while under wave conditions they lie mainly along the edge of initial overturning. Both distributions correspond to the tearing of the water tongue into jets and droplets. Among the phases, the fluctuating region at $\phi_1 = 0$ is located ahead of the bow and has a relatively small $z_{RMS}(\phi_i)$. As the phase increases, from $\phi_2 = 0.25$ to $\phi_3 = 0.5$, with jet growth and fallback, the region of intense fluctuation expands significantly and the fluctuation amplitude increases notably. By $\phi_4 = 0.75$, the jet falls back to the water surface, and the fluctuation amplitude drops sharply.

Comparing the Bottom views in Figs. 13(b) and 15, the contours of z_{Mean} and $z_{Mean}(\phi_i)$ show that air entrainment in calm water mainly appears as continuous tubular structures aligned with the flow direction, whereas under wave conditions it transforms into dispersed bubble clouds. At $\phi_1 = 0$, no obvious entrained bubble clouds are observed under wave conditions. When the phase advances to $\phi_2 = 0.25$, noticeable entrainment structures begin to appear, and their transverse position is closer to the inner side of the hull compared to calm water. As the phase further increases, the bubble clouds migrate outward and eventually distribute further outward than in calm water. From the Bottom view, the regions of high z_{RMS} and $z_{RMS}(\phi_i)$ with intense fluctuations are located at the underwater entrained cavities and bubble clouds. During the phase evolution from $\phi_1 = 0$ to $\phi_3 = 0.5$, as the initial overturning in the top view evolves and falls back, the intensity of underwater air entrainment continuously increases, until at $\phi_4 = 0.75$ it decreases as the entrainment weakens.

To quantitatively compare the differences in bow wave breaking between calm water and wave conditions, the phase of maximum wave elevation $\phi_2 = 0.25$ is selected as the representative phase. Fig. 16 presents the quantitative statistical characteristics at typical axial sections under both calm water and wave conditions at this phase. Subfigure (a) shows the axial sections where the maximum wave elevation occurs in each environment, comparing the lateral evolution of water tongue overturning at the instant of maximum wave elevation. Subfigures (b) and (c) show the sections with the maximum RMS from the Top and Bottom views under wave and calm water conditions, respectively, to quantitatively compare the dominance of jet splashing and underwater air entrainment.

As shown in Fig. 16(a), under the wave condition the maximum mean wave elevation $(z_{Mean}(\phi_2))_{\max}$ reaches 0.0587, while in calm water the corresponding $(z_{Mean})_{\max}$ is 0.0213, meaning the former is 2.75 times the latter. Considering the different far-field water levels due to waves, the actual wave elevation in the wave is 0.424, which is three times the calm-water value of 0.141. This indicates that at wave crest encounter, the instantaneous wave elevation is greatly amplified compared to calm water, requiring more energy from the hull and thus significantly increasing the wave-making resistance. Furthermore, the difference between the Top and Bottom views shows that the length of the overturning water tongue in the wave is about twice that in calm water, suggesting that jet and splash phenomena are more pronounced and dominate the bow wave breaking. From Fig. 16 (b) and 16 (c), the $(z_{RMS}(\phi_2))_{\max}$ induced by jet splashing reaches 0.0188, which is 7.83 times the value induced by underwater bubble clouds. In calm water, however, the $(z_{RMS})_{\max}$ induced by air tube oscillations is 1.84 times that induced by jet splashing. This large difference quantitatively demonstrates that under the wave condition, jet splashing has replaced air entrainment as the dominant mechanism of wave breaking, whereas air

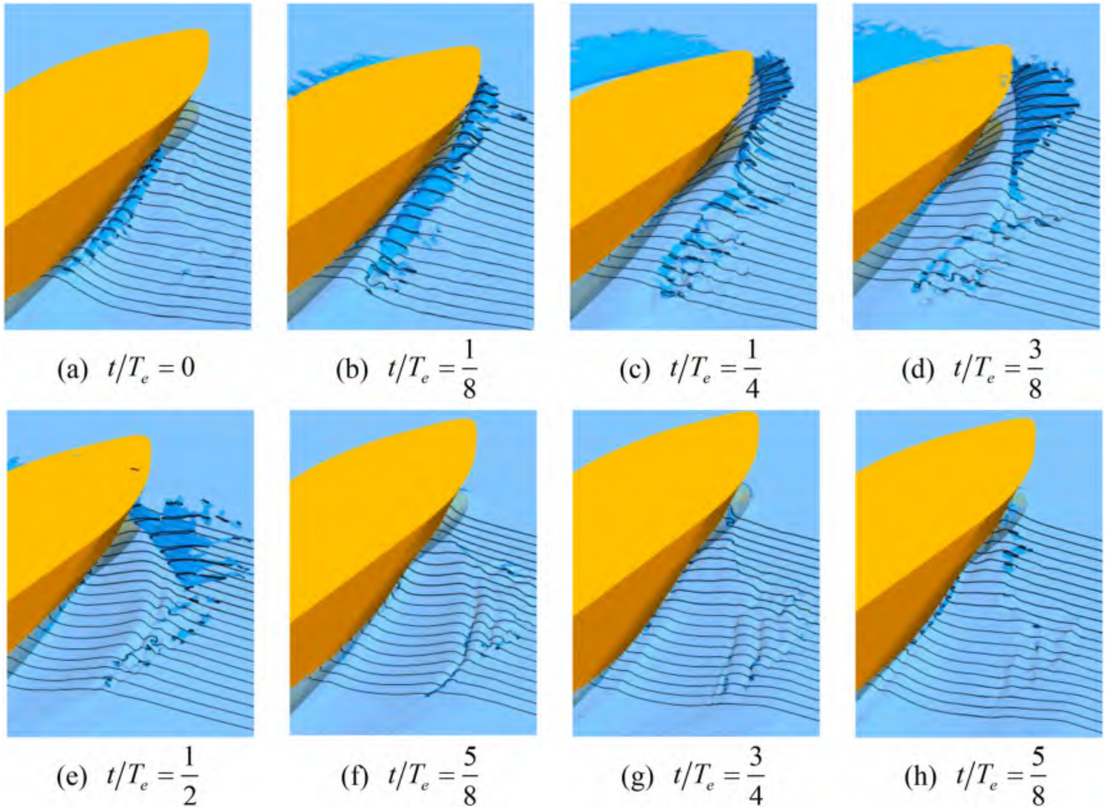

Fig. 12. Wave profiles of KCS bow wave breaking in the wave.

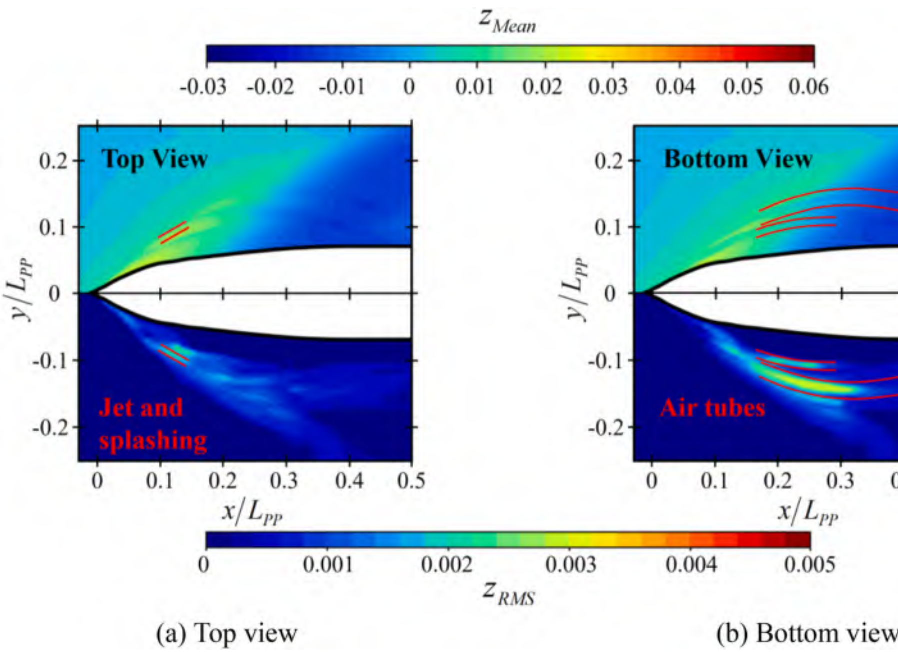

Fig. 13. Statistical characteristics of KCS bow wave breaking in calm water.

entrainment prevails in calm water. This is mainly because the wave crest significantly amplifies the wave elevation, causing the free surface to deform violently and release energy through jet fragmentation.

4.1.3. Underwater pressure field and vortex structures

Combining wave profile analysis and statistical characteristics, the differences in KCS bow wave breaking in the wave are mainly reflected in higher instantaneous wave elevation, jet splashing as the dominant breaking structure, suppression of secondary overturning, and altered morphology of entrained air. Additionally, jet splashing in calm water occurs mainly during the secondary wave breaking stage, whereas under wave conditions it already appears during the initial overturning stage. The flow mechanism of bow wave breaking is primarily the underwater pressure gradient driving the evolution of the velocity field and

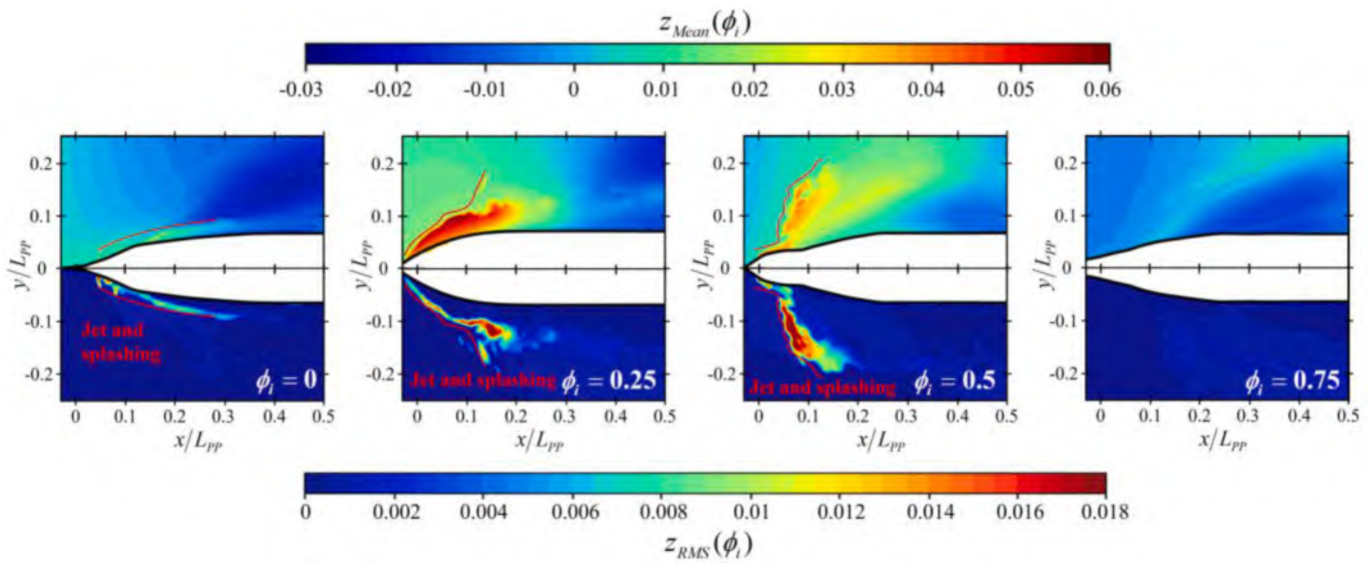

Fig. 14. Top-view phase-resolved statistics of KCS bow wave breaking in the wave.

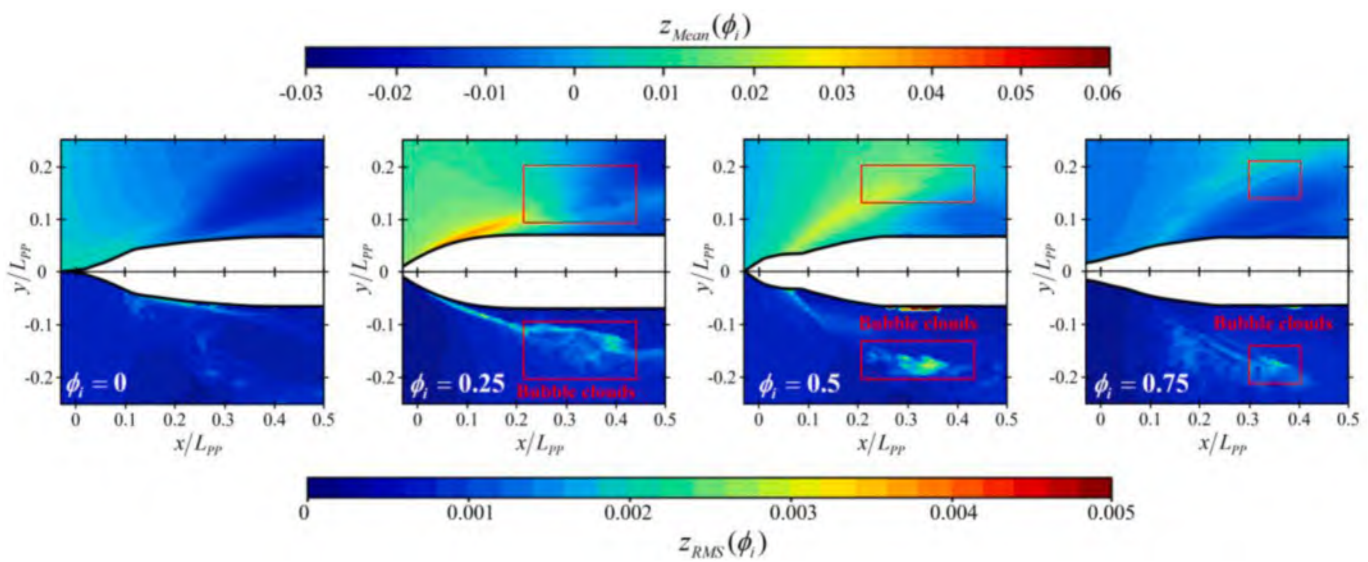

Fig. 15. Bottom-view phase-resolved statistics of KCS bow wave breaking in the wave.

generating a high-speed water tongue. Instability of the free surface triggers wave breaking phenomena such as overturning and air entrainment, while the induced vortical structures provide feedback that enhances the breaking process. Based on these mechanisms, he differences in KCS bow wave breaking behavior between the wave condition and calm water are further analyzed by examining the underwater pressure field and vortical structures.

Figs. 17 and 18 show the underwater pressure fields around the KCS in calm water and under the wave condition, respectively. The hydrostatic component has been removed. The spatial evolution is shown through a series of axial sections taken within $x \in [0.05L_{PP}, 0.3L_{PP}]$, with an interval of 0.05 L_{PP}. At $t/T_e = 0$, the positive pressure region under the wave condition has a smaller spatial extent than in calm water. However before $x = 0.15L_{PP}$, both the peak positive pressure and the pressure gradient are higher. This gives the initial overturning water tongue higher lateral and vertical velocities and a stronger shear layer, leading to intense jetting and droplet breakup already in the initial overturning stage and further intensifying these processes in later phases. Downstream of this section, the negative dynamic pressure under wave conditions is more widely distributed with a larger peak magnitude, which is associated with the bow having just passed the wave crest and the trough being near midship.

At $t/T_e = \frac{1}{4}$, the bow reaches the wave crest. The positive pressure and its extent greatly exceed calm-water levels. The water tongue is stretched upward by strong lateral velocity, lifting rather than rolling down, with extensive droplet breakup. The pressure gradient reduces vertical velocity at the tongue core, while high lateral velocity sustains outward jet expansion and lateral spreading. At $t/T_e = \frac{1}{2}$, the bow approaches the equilibrium position before the trough. The positive pressure weakens, wave elevation drops, but pressure remains above calm-water levels, so the crest continues expanding. The tongue's vertical velocity turns negative, causing a nearly vertical fallback rather than continuous overturn, hindering stable entrainment. Strong pressure gradients violently deform the tongue, leading to rapid dissipation and secondary overturning height is reduced due to fast phase transition. At $t/T_e = \frac{3}{4}$, the bow reaches the wave trough, the ship is stern-down, negative pressure dominates, water displacement nearly vanishes, and the pressure gradient is mild. Only a weak outward wave forms at the

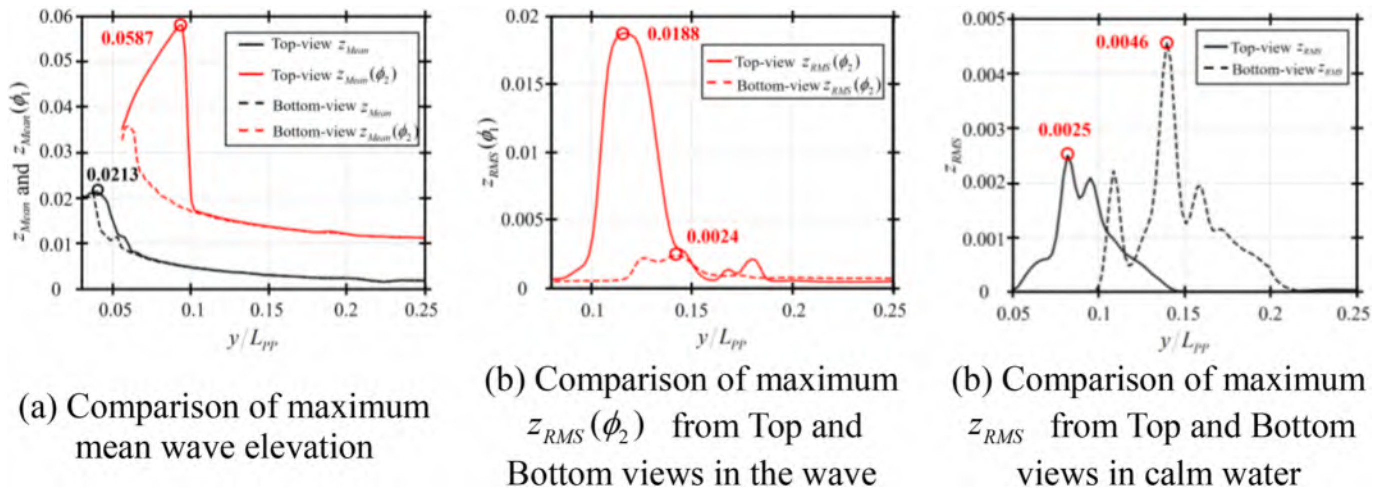

Fig. 16. Quantitative wave-height statistics at axial sections in the wave and calm water.

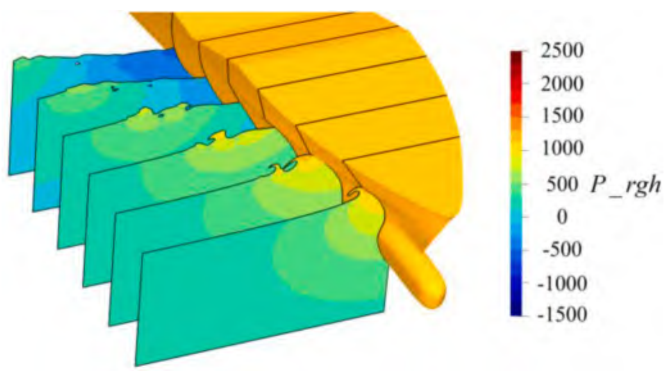

Fig. 17. Underwater pressure field around the KCS in calm water.

bow front, with gentle inward return flow downstream and overall disturbance is greatly reduced.

Underwater pressure analysis shows that strong positive pressure during the crest half-cycle creates a distinctly different wave profile. High vertical velocity greatly increases wave height, while high lateral velocity enhances jet splashing and suppresses secondary overturning by altering the fallback pattern. Rapid movement of the positive pressure region reduces water displacement, making secondary overturning and initial cavities harder to sustain, thus lowering total air entrainment compared to calm water. Consequently, stable entrainment weakens, and air entrainment shifts from continuous tubular cavities to discrete, disordered bubble clouds, with breakup intensity lower than that of jet splashing.

Figs. 19 and 20 present the underwater vortex structures in calm water and under the wave condition. In calm water the vortex structures show little variation over time. Under the wave condition they vary significantly with phase.

At $t/_{T_e} = 0$, wave-condition vortex structures are more sheet-like and fragmented than the tubular ones in calm water, intensifying initial overturning breakup and tearing the surface into jets with splashes. At $t/T_e = \frac{1}{4}$, a large negative-vorticity patch appears in the overturning region, promoting stronger upward ejection. In the air-entrainment region, calm water shows tubular counter-rotating vortices, while waves produce fragmented, entangled vortex clusters of positive and negative vorticity as shown in red boxes, increasing bubble disorder. At $t/T_e = \frac{1}{2}$, the entanglement between positive and negative fragmented vortices becomes even stronger than at $t/T_e = \frac{1}{4}$, leading to a larger $(z_{RMS}(\phi_2))_{\max}$ in the Bottom view at this phase. At $t/T_e = \frac{3}{4}$, the wave disturbance and vortical structures expand outward. Gentle secondary overturning then brings back tubular vortices similar to those in calm water. Overall, under wave conditions, vortical structures are more fragmented and show entangled positive-negative vorticity clusters in the bubble-cloud region. Fragmentation increases velocity shear and local instability, making the overturning edge more prone to tearing and splashing. Entangled clusters enhance turbulent mixing in the air-entrainment region, keeping entrained air as dispersed bubble clouds underwater.

4.2. Effects of wave steepness on bow wave breaking

4.2.1. Bow wave evolution

Wave steepness also significantly affects breaking behavior. Based on the previous comparison between calm water and wave conditions at a high Froude number of 0.35, this study shifts focus to the effect of wave steepness on model scale wave breaking. Since $\mathrm{Fr} = 0.35$ leads to excessive speed and may cause much more severe green water on deck, a lower speed $\mathrm{Fr} = 0.26$ is selected. Three cases, namely Case 3, Case 4 and Case 5, are considered with wave steepness H/λ of 0.017, 0.025 and 0.03 respectively.

Figs. 21–23 show the evolution of KCS bow wave breaking over one encounter period under different wave steepness conditions. In these figures, eight representative instants are selected within one encounter period at intervals of $\frac{1}{8}T_e$. Instantaneous wave profiles along axial sections are extracted and plotted as black solid lines. The axial range is $x \in [0.02L_{PP}, 0.4L_{PP}]$, with a spacing of 0.02 L_{PP}.

At a lower speed of $\mathrm{Fr} = 0.26$, KCS bow wave breaking follows a similar process under different wave steepnesses but shows clear asymmetry over one encounter period. During the wave crest half-cycle from $t/T_e = 0$ to $t/T_e = \frac{1}{2}$, the bow rises from equilibrium to the crest and then falls back. Heave and pitch motions differ somewhat from the $\mathrm{Fr} = 0.35$ case. The most intense breaking occurs between $t/T_e = 0$ and $t/T_e = \frac{1}{4}$, when the bow moves from equilibrium to the wave crest while the midship and stern are near the trough and crest of the previous cycle. The bow-down trim combined with the wave crest causes severe breaking. During this interval, the underwater pressure field changes more slowly than at high speed, and for the same steepness, air entrainment at $\mathrm{Fr} = 0.26$ is actually stronger than at $\mathrm{Fr} = 0.35$. Between $t/T_e = \frac{1}{4}$ and $t/T_e = \frac{1}{2}$, the wave crest lifts the bow, the stern enters the trough, the ship transitions to stern-down trim, and breaking intensity drops rapidly. During the wave trough half cycle from $t/T_e = \frac{1}{2}$ to the next $t/T_e = 0$, breaking intensity remains relatively low. The main breaking interval in this half-cycle is from $t/T_e = \frac{3}{4}$ to next $t/T_e = 0$, when the bow is at the trough and the wave crest moves aft. The forward

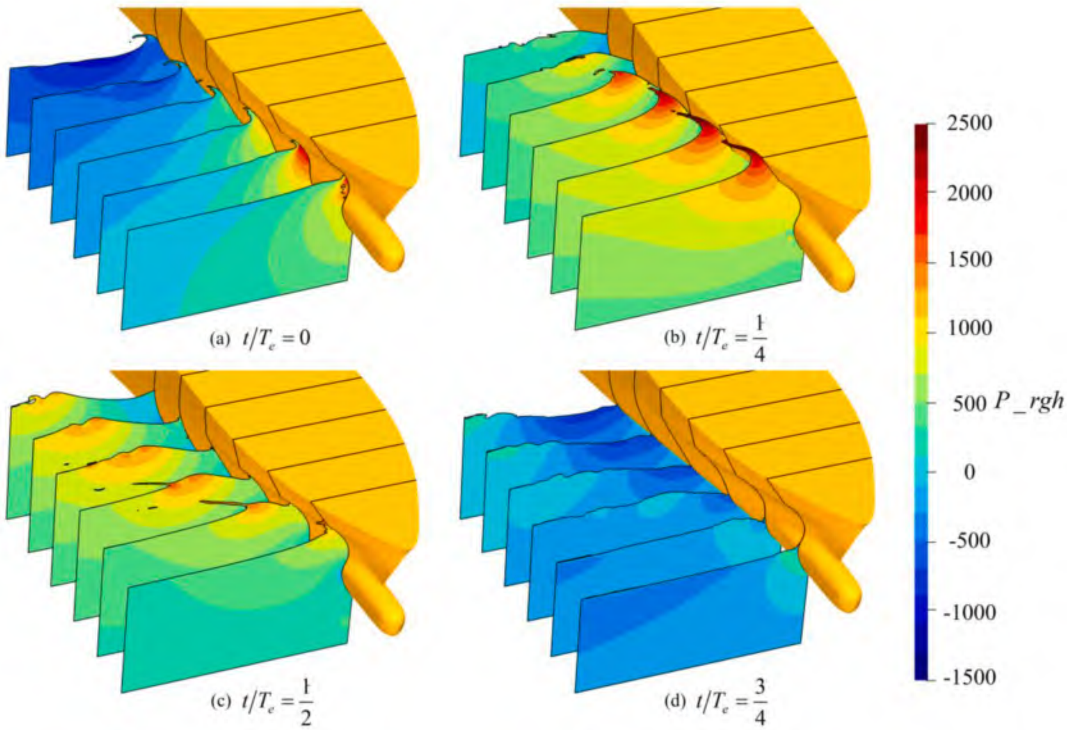

Fig. 18. Underwater pressure field around the KCS in the wave environment.

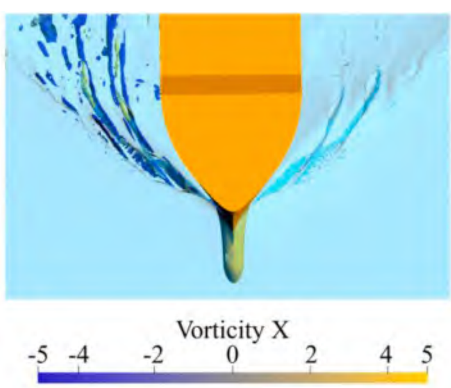

Fig. 19. Vortex structures around the KCS in the calm water.

midship presses down on the water surface first, triggering overturning.

The bow wave height from $t/T_e = 0$ to $t/T_e = \frac{1}{4}$ increases with steepness. In Case 4 and Case 5, wave breaking develops into green water on deck. All three cases show strong jet splashing and underwater air entrainment. As steepness increases, wave breaking becomes significantly stronger, with increased unsteadiness and disorder of wave profiles, stronger secondary breaking, and more jet splashing. Underwater air entrainment also becomes more chaotic, with bubble clouds appearing more random. Between $t/T_e = \frac{3}{4}$ and $t/T_e = \frac{7}{8}$, smaller steepness leads to weaker pitch and heave motions, so the water surface is pressed down earlier. Consequently, at these phases Case 3 shows earlier overturning compared with medium and high steepness cases, and at $t/T_e = \frac{7}{8}$ it exhibits noticeable secondary overturning, whereas Case 4 and Case 5 mainly show a single overturning. As steepness increases, the initial overturning region in the forward midship expands, and its unsteadiness and disorder grow significantly.

4.2.2. Bow wave height and pulsation

Based on the wave profile analysis, the wave steepness effect is quantitatively evaluated. Figs. 24 and 25 present the dimensionless phase-resolved statistics under different wave steepness conditions. The analysis focuses on the interval from $t/T_e = 0$ to $t/T_e = \frac{1}{4}$, which corresponds to the most intense wave breaking stage. Three phases $\phi_i = 0$, 0.125 and 0.25 are selected. Due to green water on deck, the analysis is limited to regions outside the deck area. The color scale for the $z_{Mean}(\phi_i)$ is set from -0.04 to 0.06 with an interval of 0.002. For the Top view, the color scale for the $z_{RMS}(\phi_i)$ is set from 0 to 0.018. For the Bottom view, the RMS color scale is set from 0 to 0.01. The interval for both RMS color scales is 0.0005.

Fig. 24 presents the phase-resolved statistical characteristics of the upper surface of KCS bow wave breaking under different wave steepnesses from the Top view. The extremely high values near the hull are caused by lateral overflow of green water and are not considered part of wave breaking, thus excluded from analysis. The contours of $z_{Mean}(\phi_i)$ show that at a fixed ship speed, wave steepness has a limited effect on the overall lateral spreading range of the wave. As the phase increases, the wave height grows rapidly and reaches its maximum at $\phi_3 = 0.25$ for all steepnesses. At $\phi_1 = 0$, the wave height does not increase monotonically with steepness, instead, it reaches its maximum under Case 4 among the three cases. However, as the phase develops to $\phi_3 = 0.25$, $z_{Mean}(\phi_3)$ becomes significantly larger under higher steepness, indicating a faster growth rate of wave elevation during the crest encounter. Moreover, with increasing steepness, the wave pattern exhibits a steeper lateral gradient and a wider lateral extent, meaning that the water tongue shows stronger lateral spreading and reaches farther transverse positions at more upstream axial sections.

High $z_{RMS}(\phi_i)$ values under all wave steepnesses are located at the fluttering edge of the water tongue, corresponding to surface tearing, elongated jets, and splashing droplets. As the phase increases, the region of high $z_{RMS}(\phi_i)$ expands rapidly, and the overall wave breaking of the water tongue intensifies significantly. For all steepnesses, the most intense jet splashing occurs at $\phi_3 = 0.25$. Comparing different steep-

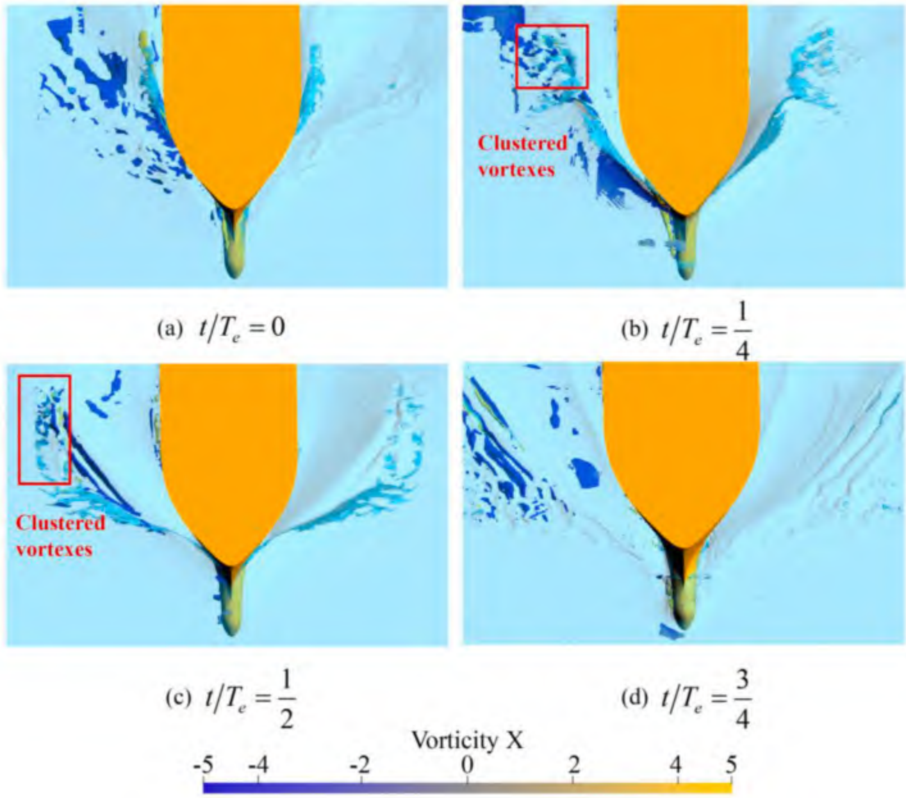

Fig. 20. Vortex structures around the KCS in the wave environment.

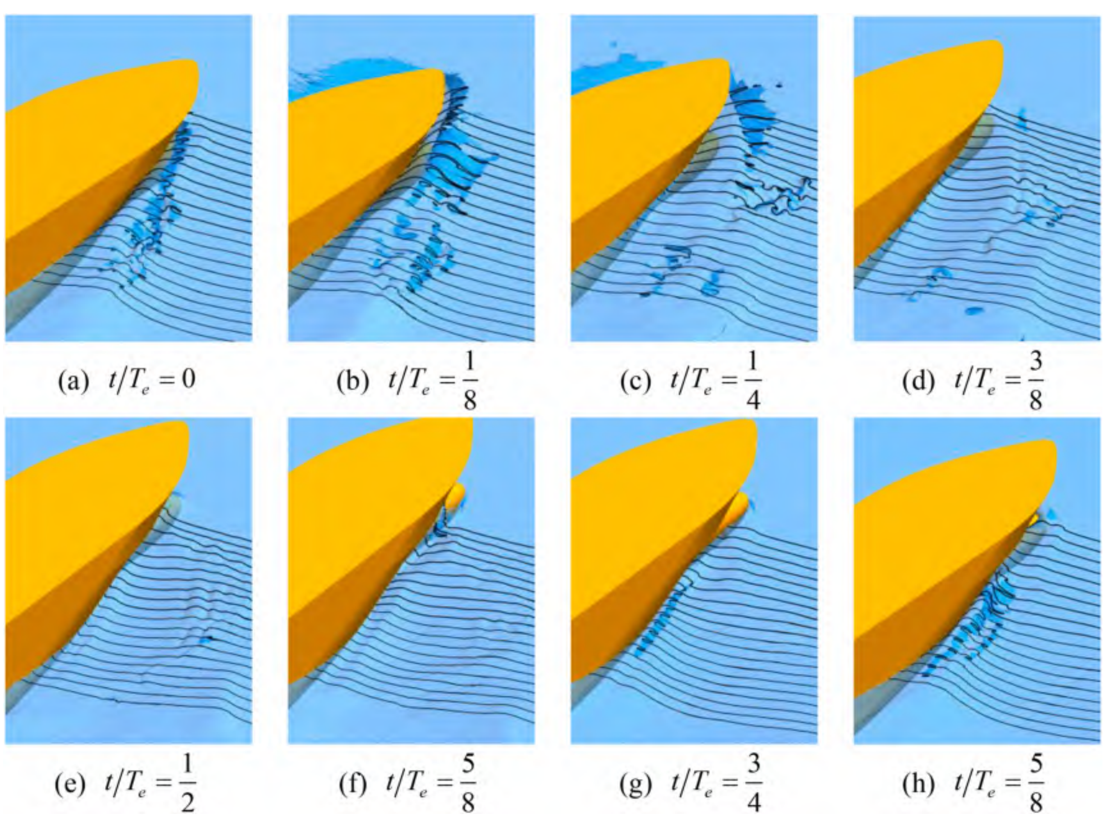

Fig. 21. Wave profiles of KCS bow wave breaking in the wave environment of $H/\lambda = 0.017$

nesses, the rapid growth rate of $z_{Mean}(\phi_i)$ under higher steepness inevitably induces violent free-surface fluctuations and instability, leading to

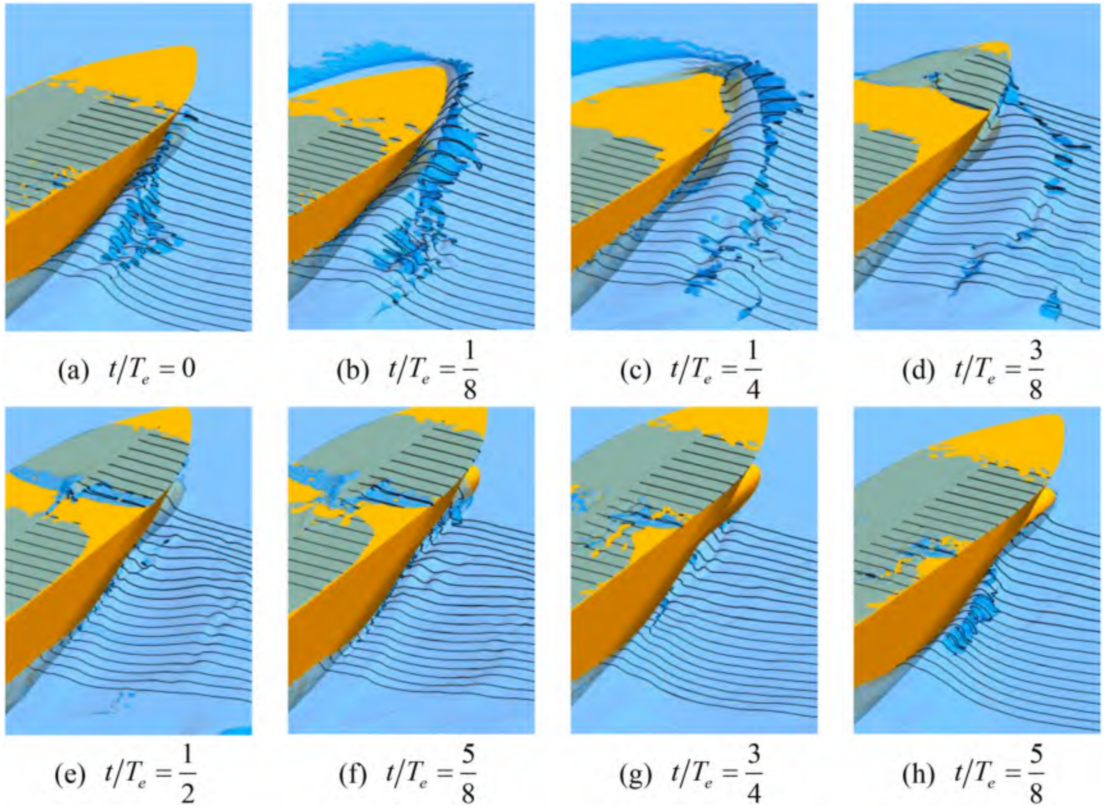

Fig. 22. Wave profiles of KCS bow wave breaking in the wave environment of $H/\lambda = 0.025$

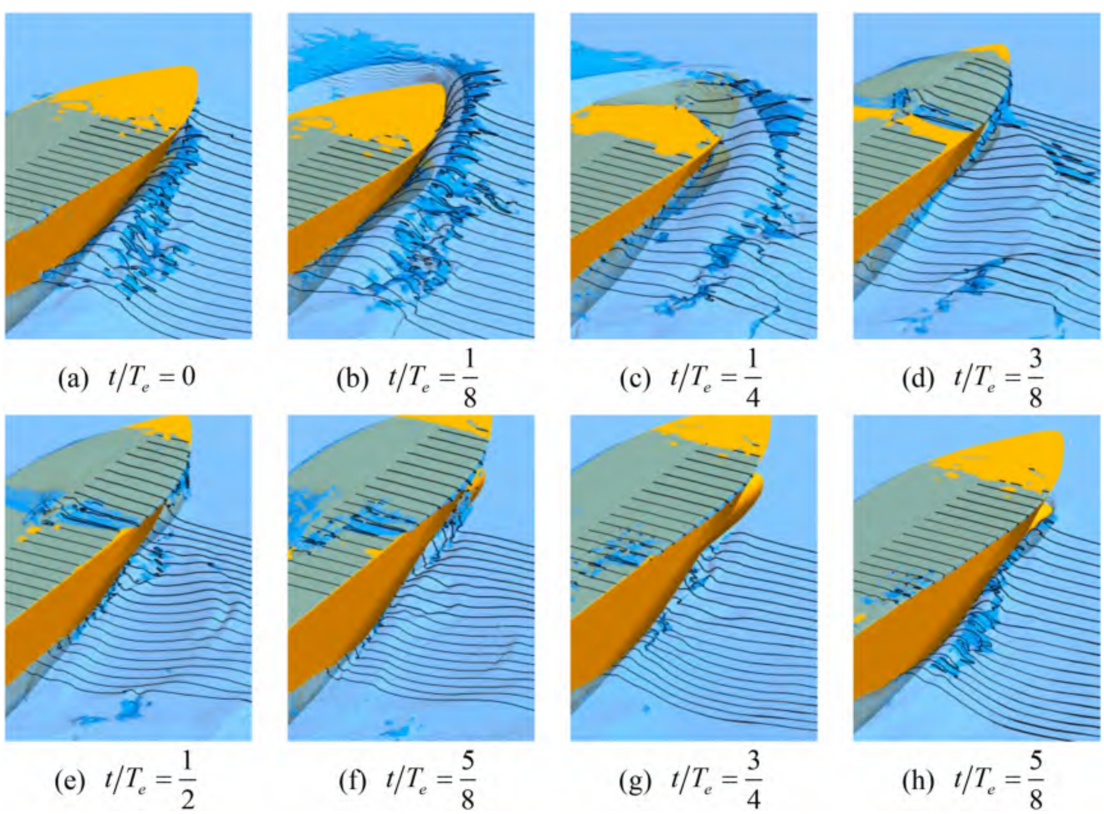

Fig. 23. Wave profiles of KCS bow wave breaking in the wave environment of $H/\lambda = 0.03$

a faster growth rate of $z_{RMS}(\phi_i)$ as well. With increasing steepness, the magnitude of $z_{RMS}(\phi_3)$ at $\phi_3 = 0.25$ increases notably, and the region of

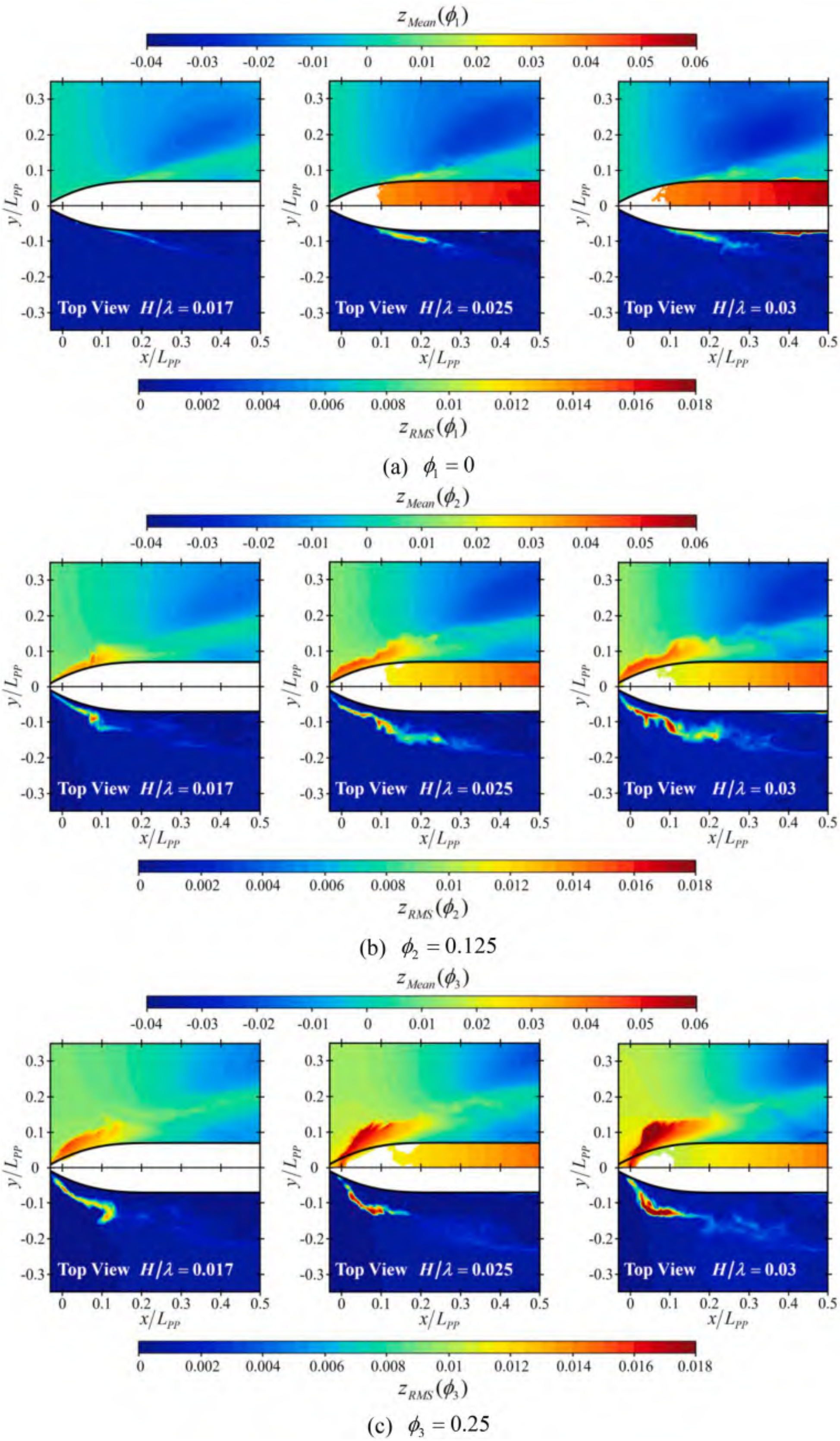

Fig. 24. Top-view statistics of KCS wave breaking with different wave steepnesses.

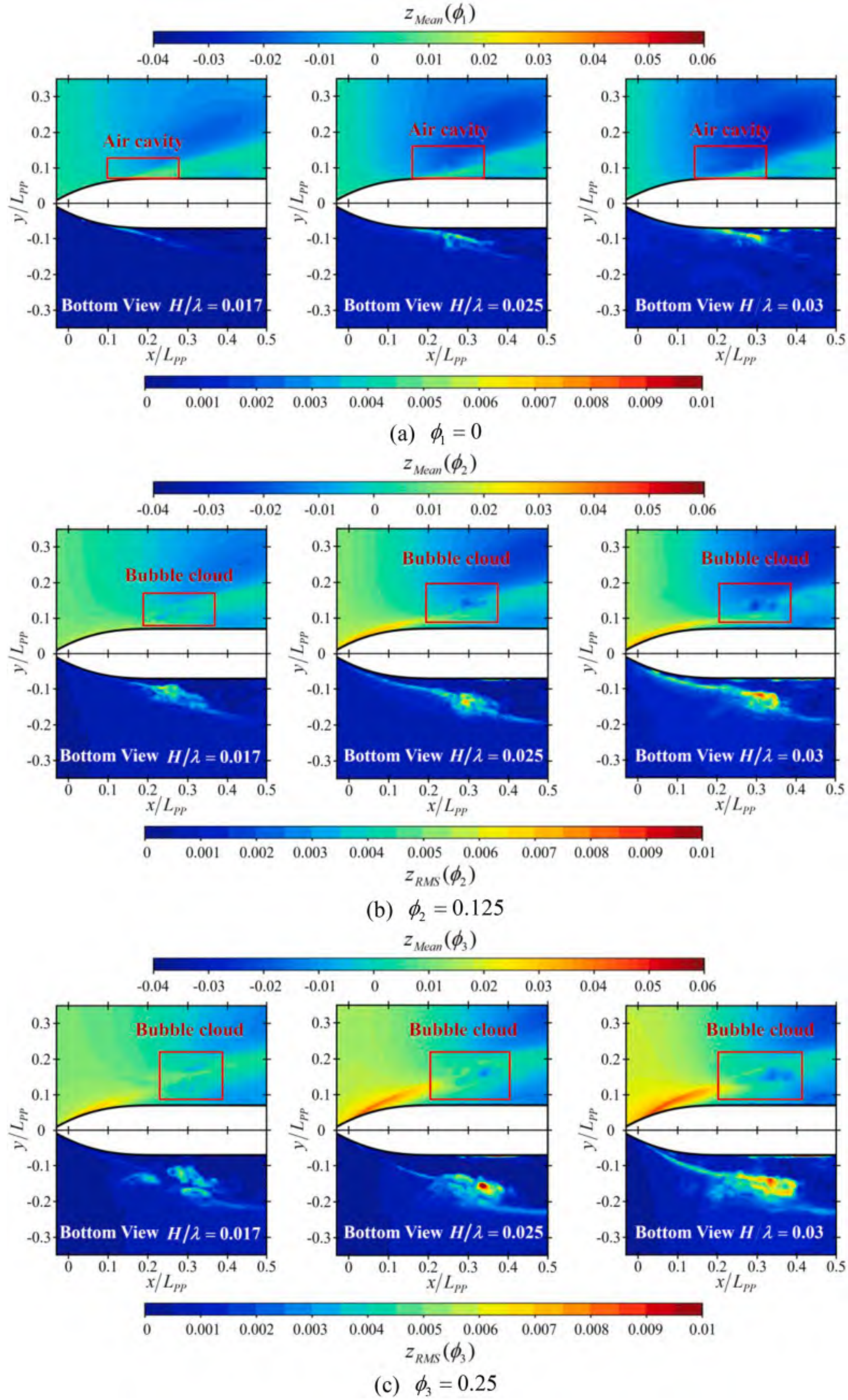

Fig. 25. Bottom-view statistics of KCS wave breaking with different wave steepnesses.

high $z_{RMS}(\phi_3)$ expands considerably, indicating that wave steepness significantly enhances the jet-splashing intensity of KCS bow wave breaking. Furthermore, at $\phi_2 = 0.125$ and $\phi_3 = 0.25$, in the region of secondary overturning and disturbed free surface downstream of section $x = 0.15L_{PP}$, the overall $z_{RMS}(\phi_i)$ increases with steepness, demonstrating that wave steepness enhances the overall breaking intensity of the free surface.

Fig. 25 presents the phase-resolved statistical characteristics of air entrainment behavior from the Bottom view under different wave steepnesses. The extremely high values near the hull are caused by surface bubble due to ship motion and are excluded from analysis. The contours of $z_{Mean}(\phi_i)$ show that wave steepness has a minor effect on the lateral distribution of underwater entrained air. However, as steepness increases, the low-$z_{Mean}(\phi_i)$ region associated with air entrainment exhibits lower values, larger volume, and longer axial extension, indicating that wave steepness significantly enhances the amount of air entrainment. The $z_{RMS}(\phi_i)$ contours show that the wave breaking intensity from the Bottom view is smaller than that from the Top view, further confirming that jet splashing dominates the wave breaking of the model under wave conditions. As the phase increases, both the magnitude and extent of high $z_{RMS}(\phi_i)$ in the underwater air-entrainment region grow, indicating that $\phi_3 = 0.25$ is also the phase where the fluctuation of underwater bubble clouds is most intense. With increasing steepness, the region of high $z_{RMS}(\phi_3)$ at $\phi_3 = 0.25$ expands significantly, demonstrating that wave steepness promotes the overall fluctuation intensity of underwater bubble clouds.

Fig. 26 further plots the lateral evolution at the most violent phase of wave breaking $\phi_3 = 0.25$, under different wave steepnesses. Subfigures (a) and (b) show the evolution of the maximum wave crest and the section with the deepest local air distribution, respectively. Considering that the horizontal plane level at this phase varies with wave steepness, color filling is used to represent the difference between the Top and Bottom views, reflecting the actual maximum wave height, the length of the overturning water tongue, and the depth of underwater air relative to the water surface. Subfigures (c) and (d) show the evolution of the axial sections where the most intense fluctuation $(z_{RMS}(\phi_3))_{\max}$ occurs in the Top and Bottom views, respectively. These characteristics are summarized in Table 8, and the variation of the average $z_{RMS}(\phi_3)$ with wave steepness is further calculated for the jet-splashing region in the Top view and the bubble-cloud region in the Bottom view. Both the maximum wave height and the maximum underwater depth are nondimensionalized by the L_{PP}.

Based on Table 8, Fig. 26(a) shows that as wave steepness increases, the maximum wave crest grows rapidly, exhibiting an approximately linear relationship with a slope of 1.58. The actual maximum wave height follows a linear trend with a slope of about 1.16. Meanwhile, the length of the overturning water tongue also increases with steepness, reaching about 1.4 times larger in Case 5 than in Case 3. This indicates that the free-surface elevation and lateral stretching become more severe, driving the increase of $(z_{RMS}(\phi_3))_{\max}$ in the Top view with steepness. The maximum underwater depth and the area between the two curves in the Bottom view provide a preliminary measure of air entrainment. As seen in Fig. 26 (b), the maximum underwater depth increases with steepness, with Case 5 about 2.04 times that of Case 3. However, the relationship is not linear, and the growth rate decreases as steepness further increases. The underwater area expands noticeably with steepness, indicating that wave steepness significantly affects the intensity of air entrainment, consistent with the earlier contour analysis.

From Fig. 26 (c), $(z_{RMS}(\phi_3))_{\max}$ is located outside the maximum wave crest. With increasing steepness, the jet-splashing $(z_{RMS}(\phi_3))_{\max}$ shows an approximately linear increase with a slope of 0.72. Comparing the ratios of maximum wave height and jet-splashing $(z_{RMS}(\phi_3))_{\max}$ between consecutive cases, the latter is always larger, suggesting that the increase in breaking intensity with steepness comes not only from higher wave elevation but also from a greater tendency of the water tongue to tear into jets and droplets. Moreover, the average $z_{RMS}(\phi_3)$ in the jet-splashing region increases with steepness, with Case 5 being about 24.5% and 5.6% higher than Case 3 and Case 4, respectively. As shown in Fig. 26 (d), the $(z_{RMS}(\phi_3))_{\max}$ of underwater bubble clouds does not increase monotonically with steepness but peaks in Case 4. Nevertheless, the average $z_{RMS}(\phi_3)$ in the bubble-cloud region increases with steepness, with Case 5 about 26.3% and 11.6% higher than Case 3 and Case 4, respectively.

4.2.3. *Underwater vortex structures*

Fig. 27 compares vortex structures and 3D wave patterns at $\phi_3 = 0.25$. With increasing steepness, vortices become more numerous and fragmented, enhancing surface disturbance. In the bow jet-overturning region, negative vortices grow in size and fragmentation, promoting jet breakup and splashing, and leading to high $z_{RMS}(\phi_3)$ along the wave edge. In the air-entrainment region, entangled vortex clusters are observed, consistent with the high $z_{RMS}(\phi_3)$ in the Bottom view. These vortex interactions induce velocity fluctuations and destabilize the entrained air, causing strong oscillations of the bubble cloud and intensifying wave breaking.

5. Conclusions

This study employs a high-fidelity DDES turbulence model and an overset-grid technique to investigate bow wave breaking of a high-speed ship under calm-water and wave conditions. The influence of wave steepness is further examined under lower speed.

First, the KCS model at Fr = 0.35 is considered. A calm-water case with a fixed trim of 1° by the bow, and a regular-wave case with steepness $H/\lambda = 0.017$ and wavelength $\lambda = 1.15\ L_{PP}$.

Wave profiles and phase-resolved wave-height statistics are used for both qualitative and quantitative comparisons. The underlying mechanisms are further interpreted using the underwater pressure field and vortex structures. The main conclusions are as follows.

(1) Bow wave breaking in waves is strongly modulated by wave phase and ship motions. Intense jetting and splashing occur already at the initial overturning stage. The water tongue spreads laterally and falls back nearly vertically, which suppresses secondary overturning and stable air entrainment. As a result, air entrainment changes from continuous cavities to dispersed bubble clouds.
(2) During the wave crest encounter, the instantaneous wave height under wave conditions is much larger than that in calm water. The peak crest and the actual wave elevation reach 2.75 and 3 times the calm-water values, respectively, and the overturning water tongue is about twice as long. The jet-splashing breaking intensity under wave conditions is 7.83 times that of the underwater bubble clouds, making it the dominant breaking structure.

Table 8
Typical statistical characteristics at $\phi_3 = 0.25$ under various wave steepnesses.

H/λ	Maximum actual bow wave height	Top-view $(z_{RMS}(\phi_3))_{\max}$	Top-view average $z_{RMS}(\phi_3)$	Maximum underwater depth	Bottom-view $(z_{RMS}(\phi_3))_{\max}$	Bottom-view average $z_{RMS}(\phi_3)$
0.017	0.0289	0.0137	0.0106	0.0075	0.0054	0.0038
0.025	0.0382	0.0193	0.0125	0.0136	0.0106	0.0043
0.03	0.0441	0.0231	0.0132	0.0153	0.0090	0.0048

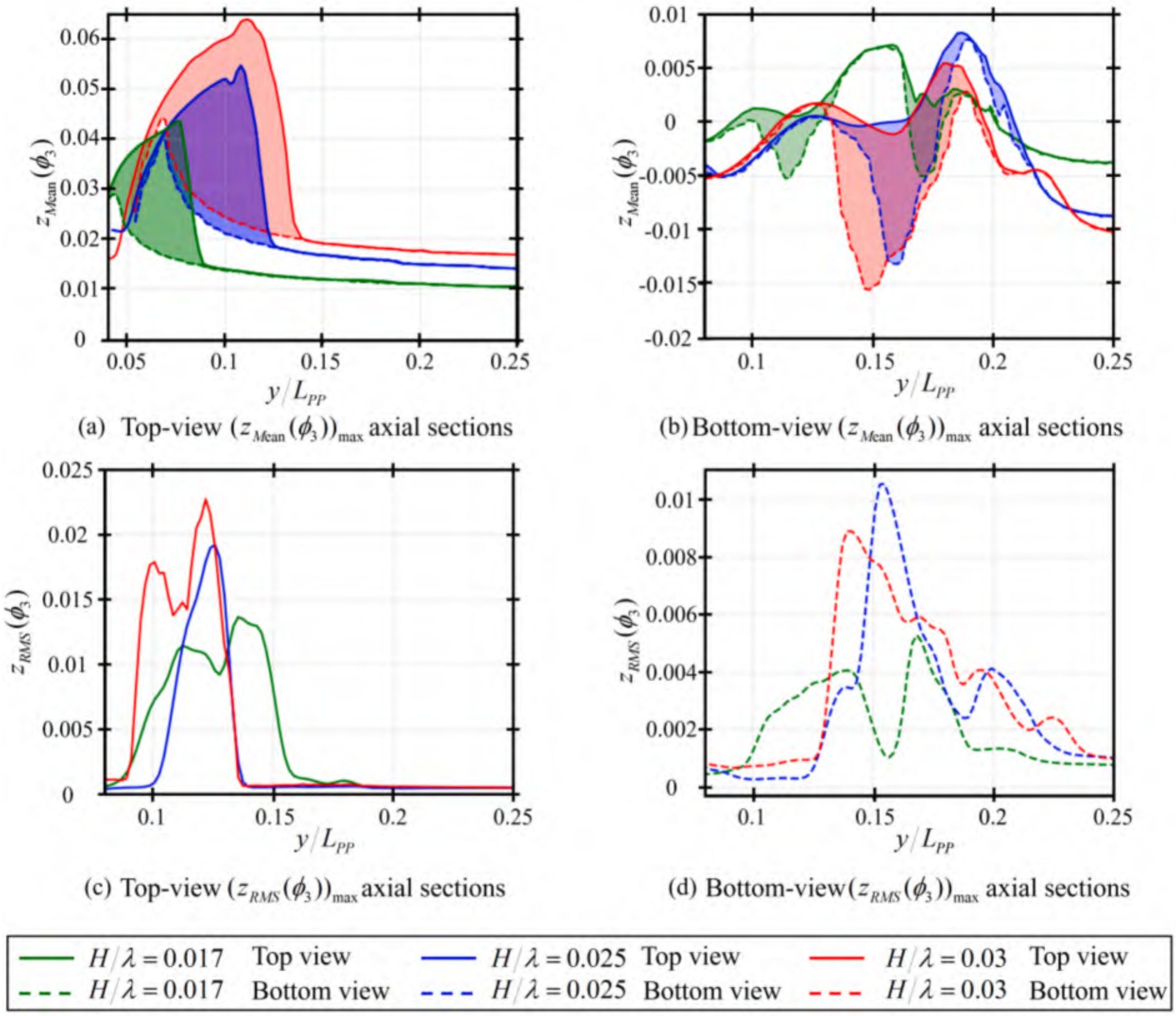

Fig. 26. Curves of statistical characteristics with wave steepness at $\phi_3 = 0.25$

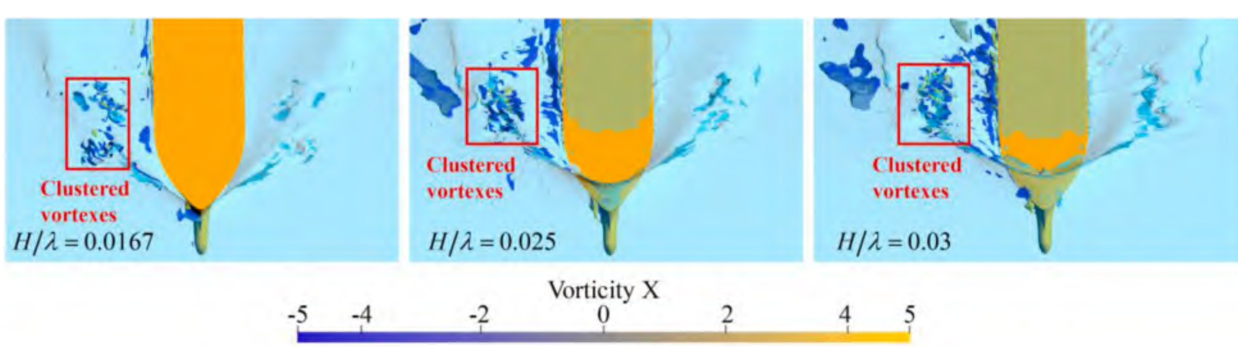

Fig. 27. Vortex structures for varying wave steepness.

(3) Under wave conditions, strong positive pressure at the crest lifts the water tongue and causes nearly vertical fallback, suppressing secondary overturning and stable air entrainment. Fragmented vortices enhance shear and free-surface instability, promoting jet tearing and droplet generation. Entrained gas remains as dispersed bubble clouds rather than continuous cavities.

Further, three wave conditions with steepness of $H/\lambda = 0.017$, 0.025 and 0.03 are investigated at Fr $= 0.26$ to examine the effect of wave steepness. The main conclusions are:

(1) Increasing wave steepness significantly enhances wave height and breaking intensity. The flow becomes more irregular, with

stronger jet–splash structures and more pronounced secondary breaking. The bubble cloud also becomes more disordered.

(2) At wave crest encounter, wave steepness significantly enhances bow wave breaking. Maximum crest height, actual wave height, and jet-splashing fluctuation increase nearly linearly with steepness, with slopes of 1.58, 1.16 and 0.72. From steepness 0.017 to 0.03, water tongue length and maximum underwater depth increase by 1.4 and 2.04 times, respectively. Overall jet-splashing intensity and bubble-cloud fluctuation rise by 24.5% and 26.3%.

(3) Higher steepness results in more fragmented vortices and larger negative vortex regions, promoting jet breakup. The interaction of vortices in the entrainment region intensifies, leading to stronger bubble-cloud oscillations.

CRediT authorship contribution statement

Wentao Wang: Data curation, Investigation, Methodology, Validation, Writing – original draft. **Xinyi Li:** Conceptualization, Data curation, Formal analysis, Investigation, Validation, Writing – original draft. **Jianhua Wang:** Formal analysis, Investigation, Resources, Software, Writing – review & editing. **Jian Xu:** Data curation, Investigation, Resources, Writing – review & editing. **Decheng Wan:** Conceptualization, Funding acquisition, Investigation, Methodology, Project administration, Software, Supervision, Writing – review & editing.

Declaration of competing interest

The authors declare that they have no known competing financial interests or personal relationships that could have appeared to influence the work reported in this paper.

Acknowledgments

This work is supported by the National Natural Science Foundation of China (Grant No. 52131102), to which the authors are most grateful.

References

Cheng, P., Wan, D., 2017. Numerical analysis of the influence of tower on wind turbine aerodynamic performance based on overset grid method. J. Hydrodyn. (1), 32–39.
Choi, B., Huijsmans, R., 2019. Experimental assessment of effects of bow-wave breaking on added resistance for the fast ship. Int. Shipbuild. Prog. 66 (3), 1–33.
Dong, R., Katz, J., Huang, T., 1997. On the structure of bow waves on a ship model. J. Fluid Mech. 346, 77–115.
Guo, H., Wang, N., Zhang, X., et al., 2023. Numerical study of motion response and wave-added resistance of KCS ship based on viscous-potential flow coupling method. Shipbuil. China 64 (1), 47–60.
Hino, T., Hirata, N., Stern, F., et al., 2020. Introduction, conclusions and recommendations. Numerical Ship Hydrodynamics: An Assessment of the Tokyo 2015 Workshop 1–21.
Hu, Y., Liu, C., Hu, C., et al., 2021. Numerical investigation of flow structure and air entrainment of breaking bow wave generated by a rectangular plate. Phys. Fluids 33 (12).
Hu, Y., Liu, C., Zhao, M., et al., 2023. High-fidelity simulation of an aerated cavity around a surface-piercing rectangular plate. Phys. Rev. Fluids 8 (4), 044003.
Iafrati, A., 2011. Energy dissipation mechanisms in wave breaking processes: spilling and highly aerated plunging breaking events. J. Geophys. Res. Oceans 116 (C7).
Karion, A., Fu, T., Waniewski, T., Rice, J., et al., 2004. Experiment to Examine the Effect of Scale on a Breaking Bow Wave[R]. Maryland: Hydromechanics Department.
Kawabuchi, M., Kawakita, C., Mizokami, S., et al., 2011. CFD predictions of bubbly flow around an energy-saving hip with mitsubishi air lubrication system. Mitsubishi Heavy Industries Techn. Rev. 48 (1), 53–57.
Li, X., Bao, F., Wang, J., et al., 2024. Spectral and statistical analysis of bow wave breaking characteristics of KCS ship. J. Hydrodyn. 36 (4), 593–608.
Li, X., Song, B., Wang, J., et al., 2025a. Multidimensional numerical analysis of wedge-shaped bow wave breaking: statistical signatures, critical frequencies, and energy distribution. Ocean. Eng. 339, 122118.
Li, X., Wang, J., Wan, D., 2025b. Frequency characteristics of KCS ship breaking bow wave[C]. 13th International Workshop on Ship and Marine Hydrodynamics. Fukuoka, Japan.
Liu, W., Wang, W., Qiu, G., et al., 2022. KCS unsteady bow wave breaking experiments for physics and CFD validation[C]. 34th Symposium on Naval Hydrodynamics (SNH). Washington DC, USA.
Lu, H., Wang, Q., He, J., et al., 2024. Binocular reconstruction of breaking ship bow waves in circulating water channel. Ocean. Eng. 300, 117426.
Mao, T., Bao, F., Wang, J., et al., 2024. Numerical study of air cavity characteristics of bow wave breaking of KCS ship under different speeds. J. Hydrodyn. 36 (4), 678–692.
Mao, T., Wang, J., Wan, D., 2025. Hydrodynamic characteristics of bow wave breaking for KCS at different yaw angles[C]. 13th International Workshop on Ship and Marine Hydrodynamics. Fukuoka, Japan.
Maxeiner, E., Shakeri, M., Duncan, J., 2011. A parametric study of breaking bow wave susing a 2D + T technique. J. Fluid Mech. 687, 540–570.
Menter, F., 1994. Two-equation eddy-viscosity turbulence models for engineering applications. AIAA J. 32 (8), 1598–1605.
Noblesse, F., Delhommeau, G., 2013. Ship bow waves. J. Hydrodynamics, Ser. B 25 (4), 491–501.
Pogozelski, E., Katz, J., Huang, T., 1997. The flow structure around a surface piercing strut. Phys. Fluids 9, 1387–1399.
Roth, G., Mascenik, D., Katz, J., 1999. Measurements of the flow structure and turbulence within a ship bow wave. Phys. Fluids 11, 3512–3523.
Shao, Y., Song, B., Wang, J., et al., 2025. Wave breaking characteristics around a wedge-shaped bow: high-fidelity simulation of water–air–bubble mixed flow. Phys. Fluids 37 (7).
Spalart, P., Deck, S., Shur, M., et al., 2006. A new version of Detached-eddy simulation, resistant to ambiguous grid densities. Theor. Comput. Fluid Dynam. 20 (3), 181.
Strelets, M., 2001. Detached eddy simulation of massively separated flows. AIAA J. 1–18.
Sun, B., 2023. Numerical Investigation of Bow Wave Breaking and Ship Motion Responses Under Strongly Nonlinear Waves at Medium and High Speeds[D]. Harbin Engineering University.
Wang, J., Wang, W., Wan, D., 2023. Scale effects on bow wave breaking of KCS ship model: insights from DDES investigations. J. Hydrodyn. 35 (4), 668–678.
Wang, Z., Yang, J., Stern, F., 2010. Numerical simulations of wave breakings around a wedge-shaped bow[C]. 28th Symposium on Naval Hydrodynamics. Pasadena, California.
Waniewski, T.A., Brennen, C.E., Raichlen, F., 2001. Measurements of air entrainment by bow waves. J. Fluids Eng.Trans. Asme. 123, 57–63.
Wilson, R., Carrica, P., Stern, F., 2006. URANS simulations for a high-speed transom stern ship with breaking waves. Int. J. Comput. Fluid Dynam. 20, 105–125.
Wilson, R., Carrica, P., Stern, F., 2007. Simulation of ship breaking bow waves and induced vortices and scars. Int. J. Numer. Methods Fluid. 54 (4), 419–451.
Wu, D., 2022. Investigation of Fine Flow Field and Hydrodynamic Performance of Bow Wave Breaking for Standard Ship Models Based on DDES Method[D]. Shanghai Jiao Tong University.
Wu, D., Wang, J., Wan, D., 2020. Numerical simulation of bow wave breaking for a high-speed DTMB ship model using CFD method[C]. 31st National Conference on Hydrodynamics, Fujian, China.
Wyatt, D., Fu, T., Taylor, G., et al., 2008. A comparison of full-scale experimental measurements and computational predictions of the transom-stern wave of the R/V athena I[C]. 27th Symposium on Naval Hydrodynamics (SNH), Seoul, KOREA.
Xie, L., Wang, J., Wan, D., 2021. Numerical investigation of scale effects on bow wave breaking using DDES method. Shipbuil. China 62 (2), 82–96.
Ye, H., Shen, Z., Wan, D., 2012. Numerical simulation of added resistance and motion responses for DTMB 5512 ship in waves[C]. 17th International China Boat Show and High-Performance Marine Vehicles Academic Conference. Shanghai, China.
Zhang, X., He, K., Wan, D., 2022. Research progress on the mechanisms of bubbly flows and numerical simulation methods for marine structures. Chinese J. Ship Res. 17 (3), 1–28.